arXiv:2302.04227v1 [cond-mat.soft] 8 Feb 2023

Reduced-order approach for soft material inertial cavitation rheometry

Z. Zhu,[1, a)] B. Abeid,[1] and J.B. Estrada[1]
Department of Mechanical Engineering, University of Michigan, Ann Arbor, MI, United States

(Dated: 9 February 2023)

An understanding of inertial cavitation is crucial for biological and engineering applications such as non-invasive tissue surgeries and the mitigation of potential blast injuries. However, predictive modeling of inertial cavitation in biological tissues is hindered by the difficulties of characterizing fluids and soft materials at high strain rates, and the computational cost of calibrating biologically-relevant viscoelastic models. By incorporating a reduced-order model of inertial cavitation in the inertial microcavitation rheometry (IMR) experimental technique, we present an efficient procedure to inversely characterize viscoelastic material subjected to inertial cavitation. Instead of brute-force iteration of constitutive model parameters, the present approach directly estimates the elastic and viscous moduli according to the size-dependent scaling of bubble dynamics. Through reproduction of numerical-simulated inertial cavitation kinematics and experimental characterization of benchmark materials, we demonstrate that the proposed framework can determine the complex rate-dependent properties of soft solid with a small number of numerical simulations. The availability of this procedure will broaden the applicability of IMR for localized characterization of fluids and soft biological materials at high strain rates.

I. INTRODUCTION

Inertial cavitation is the process in which a bubble experiences rapid, unsteady expansion and collapse due to abrupt pressure changes. Initially studied in the context of fluids and hydrodynamics applications, accurate modeling of inertial cavitation required models incorporating significant governing physics to be predictive, leading to incorporation of pressure gradients[1], weakly compressible behavior[2], heat[3] and mass transfer[4], non-linear oscillations[5], and other fluid constitutive properties[6–8]. As the application space of inertial cavitation theory continued to evolve, soft solids with significant fluid content (such as those in the human body) became an important application space, particularly in the contexts of high-rate injury and ultrasound-based tissue surgery. For example, if the human body is subjected to a ballistic, blast, or crash event, inertial cavitation is a cause of finite, high-rate deformation and damage in soft tissues[9,10]. In recent years, inertial cavitation has also been carefully harnessed to achieve targeted tissue destruction in the form of shock wave lithotripsy[11] and histotripsy[12,13]. To effectively navigate the boundary between beneficial medical procedures and harmful cavitation-induced injuries, an understanding of the bubble-soft tissue interaction is not only important, but must be understood well-enough to adjust a procedure in near-real time. Fortunately, we can leverage the past incorporation of viscoelastic fluid (which we will refer to generally as soft material) behavior into modeling inertial cavitation dynamics as a starting point.

The inertial cavitation problem is commonly modeled by a system of governing equations including conservation of energy, mass, and momentum. Depending on the complexity of the material and bubble behavior, simplifications may be made. Incorporating appreciable material compressibility requires directly solving the balance of mass, energy, and momentum in the material-plus-bubble system, performed well in practice using interface-capturing methods[14–16]. Higher-order accurate numerical methods, e.g., Weighted Essentially Non-Oscillatory (WENO) methods[17], have been applied to capture nonlinear waves (e.g., shocks) for high-fidelity bubble dynamic simulations in a liquid [18–20] and near surface[21]. Phase change at the bubble-material interface has been incorporated with the use of fully-Eulerian Multi-component Flow Code (MFC) and a high-order accurate, shock- and interface-capturing numerical solver[19,22]. Three-dimensional

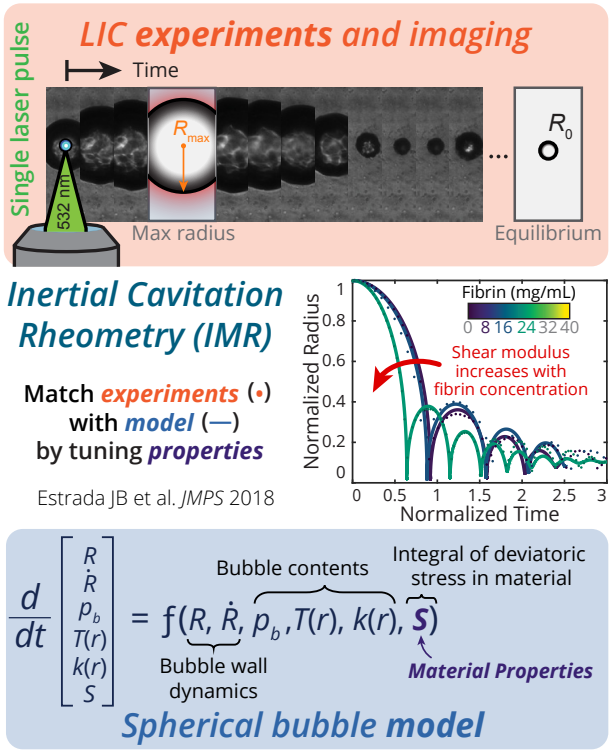

FIG. 1. Inertial microcavitation rheometry (IMR) combines laser-induced cavitation (LIC) experiments with a Rayleigh-Plesset-like model incorporating material behavior to inversely determine finite, high-rate viscoelastic material properties.

[a)] Now at School of Engineering, Brown University, Providence, RI, USA.

fluid-structure interactions and multi-scale cavitation dynamics with linear elastic bubble surroundings has also been achieved with MFC [23].

In material systems well-modeled by limited compressibility and relatively low Mach numbers during bubble collapse, this set of governing equations reduces to a 1D spherical problem. In the fully incompressible case, momentum is described by the well-known Rayleigh-Plesset equation[1,24], while incorporation of limited compressibility leads to the Keller-Miksis[2] relation.

Embedded in the Keller-Miksis equation is a driving pressure differential, which in turn relies on the integral of the stress field in the material. Thus, our description of inertial cavitation in soft biological tissues further requires an understanding of the associated finite viscoelastic behavior at high rates. In general, this is a challenge; biological materials are notoriously difficult to characterize due to a confluence of experimental challenges including a high level of compliance, spatial heterogeneity and rate-dependence of mechanical properties, and drastically different behaviors between *ex-* and *in-vivo* samples. Past efforts to model the inertial cavitation in soft tissues and polymeric materials have ranged from simple, linear viscoelastic models[25,26] to models accounting for nonlinear viscosity[27,28] and nonlinear elasticity[29,30].

To incorporate biomechanically relevant viscoelastic models in the prediction of material response to inertial cavitation, a robust experimental characterization procedure is necessary to calibrate those constitutive models. Pressure-induced cavitation rheology was introduced by Crosby and co-workers as an approach to probe the local elastic properties of soft materials. A cavity of air or immiscible liquid is injected in the characterized media via a syringe pump and the elastic modulus is determined according to the pressure and bubble radius at the onset of mechanical instability. The technique has been successfully applied to characterize elastic modulus and surface energy of soft matter including gels[31,32], biological tissues[33], and individual cell spheroids[34]. Extensions of the the pressure-induced cavitation rheology have been developed in recent years to investigate dynamic fracture[35,36] and viscoelasticity at moderate strain rates up to 1 s^{-1} [37]. However, the applicability of these techniques to characterize material viscoelasticity at a higher range of strain rates is limited by the increased contribution from inertia and cavity asymmetry not captured by the governing theories.

The inertial microcavitation rheometry (IMR) technique as illustrated in Figure 1 has been demonstrated as a powerful alternative approach to characterize the local, rate-dependent properties of soft materials subjected to finite deformation at high strain rates exceeding 10^{-3} s^{-1} [30,38]. In this approach, a laser-induced cavity is generated in a soft, transparent hydrogel or liquid and the bubble kinematics are recorded by an ultra-high-speed camera. Coupled with the Keller-Miksis-based spherical inertial cavitation bubble model developed by Johnsen and coworkers[28,29,39], the viscoelastic properties of the cavitated media are inversely characterized for a chosen material model. As is typical for inverse characterization techniques, IMR requires extensive numerical simulations to achieve calibration of material parameters. Simulations according to the inertial cavitation bubble model are repeated with varying material properties until the simulated bubble kinematics achieve a least-squares minimum in comparison to the experimental measurement. The computational portion of this framework becomes increasingly time-consuming for complex viscoelastic models, as the required number of simulations scales exponentially with the number of independent parameters in the constitutive model. Yet, soft polymers and tissues typically display viscoelastic behaviors that cannot generally be captured by the simple Kelvin-Voigt models used in our prior work[38]. The presence of complex microstructural features in the materials contribute to multiple inherent time scales and typically require a multi-term Maxwell rheological model with additional parameters per timescale[37,40]. The inverse characterization of such advanced viscoelastic models cannot realistically proceed in a brute-force manner.

The present study approaches the aforementioned challenges by presenting a reduced-order approach to IMR. Based on the observation that elastic effects in inertial cavitation are independent of bubble size while viscous effects are amplified at smaller length scales, an initial estimate of material parameters is obtained with a small number of simulations for only the first oscillatory cycle of the cavitation process. Additionally, a subset of Schlieren imaging is incorporated in the experimental procedure to capture shock wave formation during the high-speed initial collapse of the cavitated bubble, thereby improving the time resolution for the estimated duration of the initial collapse. The effectiveness of this approach is illustrated with reproduction of numerically-simulated inertial cavitation kinematics and accelerated experimental characterization of benchmark materials.

II. THEORY AND METHODS

A. Theoretical framework of bubble dynamics

The inertial cavitation dynamics is described with a theoretical framework established in our previous work[38]. Briefly, we consider the ensuing time evolution of a spherically symmetric bubble with limited compressibility, which is described by the Keller-Miksis equation [2,38,39], i.e.:

$$\left(1-\frac{\dot{R}}{c}\right)R\ddot{R}+\frac{3}{2}\left(1-\frac{\dot{R}}{3c}\right)\dot{R}^2 = \frac{1}{\rho}\left(1+\frac{\dot{R}}{c}\right)\left(p_b-\frac{2\gamma}{R}+S-p_\infty\right)+\frac{1}{\rho}\frac{R}{c}\overline{\left(p_b-\frac{2\gamma}{R}+S\right)}^{\cdot}, \tag{1}$$

where $R(t)$ is the evolving bubble radius; overdots denote derivatives with respect to time; ρ is the mass density of the surrounding material, which is assumed to be constant; c is the longitudinal wave speed, which is assumed to be constant and equal to the speed of sound in water; γ is the surface tension between the gaseous bubble contents and the surrounding medium; p_b is the internal bubble pressure; $p_\infty(t)$ is the far-field pressure, which is assumed to be atmospheric; and S is

the stress integral of the deviatoric Cauchy stress $\mathbf{s}$ in the surrounding material, which is generally defined as:

$$S = \int_R^\infty \frac{2}{r}\left(s_{rr} - s_{\theta\theta}\right) dr, \tag{2}$$

where s_{rr} and $s_{\theta\theta}$ are the radial and polar components of $\mathbf{s}$, respectively. The deviatoric part of Cauchy stress is defined as $\mathbf{s} = \sigma + p\mathbf{I}$, where σ is the total Cauchy stress and $p = -\mathrm{tr}\left(\sigma\right)$ is the hydrostatic pressure.

The initial growth phase of the bubble involves complex plasma physics causing significant thermodynamics changes inside the bubble[41]. Rather than model this process directly, the initial growth phase is only considered insofar as providing a reference state and experimentally informed growth rate for the material. As in our prior work, we use the approximated state of the bubble at maximum expansion (i.e., the bubble is at ambient temperature and homobaric) and the amount of non-condensible gas at equilibrium to inform the remaining initial model parameters[38].

1. Finite deformation constitutive equations for the surrounding medium

The deformation kinematics of the viscoelastic medium surrounding the bubble is treated in a similar manner as in our previous work[38]. We denote the equilibrium radius of the spherical bubble as R_0 and the referential radial coordinate for a material point in the medium to be r_0, where $r_0 \in [R_0, \infty)$, is measured from the center of the bubble. The time-dependent radius of the bubble wall is denoted as $R(t)$, while the deformed coordinate of a material point r_0 is denoted as $r(r_0, t)$. Near-field incompressibility and spherical symmetry is assumed. Introducing the hoop stretch, $\lambda = r/r_0$, we have the deformation gradient

$$[\mathbf{F}] = \begin{bmatrix} \lambda^{-2} & 0 & 0 \\ 0 & \lambda & 0 \\ 0 & 0 & \lambda \end{bmatrix}, \tag{3}$$

and the following incremental relation [38,42]:

$$\frac{dr}{r} = \frac{d\lambda}{\lambda(1-\lambda^3)}. \tag{4}$$

The stress field $\mathbf{s}$ and spatial stress integral S resulting from the above deformation field varies according to the constitutive model assumed. Constitutive models considered in the present study are discussed below. Schematics of the constitutive models are presented in Figure 2.

a. Finite-deformation Kelvin-Voigt model The finite deformation Kelvin-Voigt model consists of a Neo-Hookean elastic response in parallel with a Newtonian viscous response. The deviatoric stress response to material deformation is additively decomposed into elastic and viscous parts, $\mathbf{s} = \mathbf{s}^e + \mathbf{s}^v$. This allows us to additively construct the stress integral term in the Kelvin-Voigt equation.

For an incompressible Neo-Hookean elastic material, we consider the strain energy density function

$$\psi(\mathbf{F}) = \frac{G}{2}\left[\mathrm{tr}\left(\mathbf{F}\mathbf{F}^T\right) - 3\right], \tag{5}$$

where G is the ground-state shear modulus. The non-zero components of the elastic deviatoric stress $\mathbf{s}^e$ are then

$$s^e_{rr} = -2s^e_{\theta\theta} = \frac{2G}{3}\left[\lambda^{-4} - \lambda^2\right]. \tag{6}$$

Then, using Equation 4 to perform a change of variables, the stress integral defined in Equation 2 is evaluated for the Neo-Hookean elastic medium:

$$\begin{aligned} S^e &= 2G\int_{R/R_0}^1 \left(\lambda^{-5} - \lambda^{-2}\right) d\lambda \\ &= \frac{G}{2}\left[\left(\frac{R_0}{R}\right)^4 + 4\frac{R_0}{R} - 5\right]. \end{aligned} \tag{7}$$

For an incompressible Newtonian fluid, the Cauchy stress is expressed as

$$\sigma = 2\mu\mathbf{D} - p_0\mathbf{I}, \tag{8}$$

where μ is the viscous shear modulus, p_0 is a hydrostatic pressure, and $\mathbf{D}$ is the rate of deformation tensor:

$$\mathbf{D} = \frac{1}{2}\left(\dot{\mathbf{F}}\mathbf{F}^{-1} + \mathbf{F}^{-T}\dot{\mathbf{F}}^T\right), \tag{9}$$

Noting that $\mathrm{tr}(\mathbf{D}) = 0$, the non-zero components of the viscous deviatoric Cauchy stress $\mathbf{s}^v = \sigma - \mathrm{tr}\left(\sigma\right)\mathbf{I}$ are then

$$s^v_{rr} = -2s^v_{\theta\theta} = -\frac{4\mu\dot{R}R^2}{r^3}. \tag{10}$$

The corresponding viscous contribution to the stress integral is then:

$$S^v = -\frac{4\mu\dot{R}}{R} \tag{11}$$

Combining the elastic and viscous contributions, the overall stress integral in the finite deformation Kelvin-Voigt material is

$$S = S^e + S^v = \frac{G}{2}\left[\left(\frac{R_0}{R}\right)^4 + 4\frac{R_0}{R} - 5\right] - \frac{4\mu\dot{R}}{R} \tag{12}$$

b. Standard nonlinear solid model The standard nonlinear solid model is a finite deformation generalization of the standard linear solid model, consisting of a Neo-Hookean elastic response in parallel with a Maxwell element. The Neo-Hookean component corresponds to a ground-state equilibrium response, while the Maxwell component generates a non-equilibrium, time-dependent stress response with fading memory. The deviatoric Cauchy stress is again additively decomposed into equilibrium and non-equilibrium parts, $\mathbf{s} = \mathbf{s}^{eq} + \mathbf{s}^{neq}$.

Schematically, a Maxwell element consists of an elastic spring in series with a viscous dashpot. Under finite deformation, this results in a deformation gradient multiplicatively decomposed into elastic and viscous parts, i.e.:

$$\mathbf{F} = \mathbf{F}^e\mathbf{F}^v, \tag{13}$$

which leads to a scalar decomposition of hoop stretch $\lambda = \lambda^e\lambda^v$ for the cavitation problem considered in the present study.

For ease of mathematical manipulation, we introduce the logarithmic Hencky strain [43–45]:

$$\mathbf{E}^e = \frac{1}{2}\ln\left(\mathbf{F}^{eT}\mathbf{F}^e\right) \tag{14}$$

and, accordingly, express the free energy density function of the elastic spring as

$$\psi\left(\mathbf{E}^e\right) = G_1|\mathrm{dev}\left(\mathbf{E}^e\right)|^2, \tag{15}$$

where G_1 is the associated shear modulus of the elastic Hencky spring. The non-zero components of the deviatoric Cauchy stress are:

$$s_{rr}^{neq} = -2s_{\theta\theta}^{neq} = -4G_1\ln\lambda^e. \tag{16}$$

For the viscous part of the Maxwell element, we adopt the Newtonian fluid formulation presented in Equation 10, with viscous modulus again written as μ. Given stress equivalence in the elastic and viscous parts of the Maxwell element, we have the following relationship between the elastic, viscous, and total stretch:

$$\frac{\dot{\lambda}}{\lambda} - \frac{\dot{\lambda}^e}{\lambda^e} = \frac{1}{\tau_1}\ln\lambda^e \tag{17}$$

where $\tau_1 = \mu/G_1$ is an inherent time scale describing the relaxation of the Maxwell element. Equation 17 can be rewritten in the form of stress evolution:

$$\dot{s}_{\theta\theta}^{neq} + \frac{1}{\tau_1}s_{\theta\theta}^{neq} = 2G_1\frac{\dot{\lambda}}{\lambda}, \tag{18}$$

To obtain the stress integral, we perform the following operation on the stress evolution equation:

$$\begin{aligned}
\frac{d}{dt}\left(e^{t/\tau_1}s_{\theta\theta}^{neq}\right) &= e^{t/\tau_1}\left[\frac{s_{\theta\theta}^{neq}}{\tau_1} + \dot{s}_{\theta\theta}^{neq}\right] \\
s_{\theta\theta}^{neq}(t) &= \int_{-\infty}^{t} e^{(z-t)/\tau_1}\left[\frac{s_{\theta\theta}^{neq}(z)}{\tau_1} + \dot{s}_{\theta\theta}^{neq}(z)\right]dz \\
s_{\theta\theta}^{neq}(t) &= -4G_1\int_{-\infty}^{t} e^{(z-t)/\tau_1}\left(\frac{\dot{\lambda}(z)}{\lambda(z)}\right)dz
\end{aligned} \tag{19}$$

Accordingly, the stress integral in the Keller-Miksis equation can be evaluated for the Maxwell element:

$$S^{neq} = -12G_1\int_R^{\infty}\frac{1}{r(t)}\left[\int_{-\infty}^{t} e^{(z-t)/\tau_1}\frac{v_r(z)}{r(z)}dz\right]dr, \tag{20}$$

where $v_r(z)$ is the radial velocity. It can be seen from Equation 20 that the Maxwell element experiences an exponentially decaying stress response to deformation. During the characteristic time scale of τ_1, the stress response to an instantaneous strain drops to $1/e$ of its initial value. The numerical evaluation of the stress integral is discussed further in the Numerical Methods section.

c. Fractional viscoelasticity Another form of material with fading memory is the fractional viscoelastic "springpot". This model reflects a power-law viscoelastic response corresponding to a broad, continuous distribution of relaxation time scales in the material[40]. The fractional Kelvin-Voigt model, consisting of a Neo-Hookean spring and a fractional viscoelastic springpot in parallel, has previously been applied to model gels[46–48] and biological tissues[49–51]. Similar to the standard nonlinear solid model, the deviatoric Cauchy stress in the fractional Kelvin-Voigt model is additively decomposed into equilibrium and non-equilibrium parts, $\mathbf{s} = \mathbf{s}^{eq} + \mathbf{s}^{neq}$.

Here we adopt the Caputo definition of fractional derivative[52,53]:

$$D^{\alpha}y(t) = \frac{d^{\alpha}}{dt^{\alpha}}y(t) = \frac{1}{\Gamma(1-\alpha)}\int_{-\infty}^{t}\frac{d}{ds}y(s)(t-s)^{-\alpha}ds, \tag{21}$$

which exhibits a form of convolution integral similar to the governing equation of the aforementioned Maxwell element, with a power law function describing the fading memory.

We consider a finite viscoelasticity model based on this concept of fractional derivative, previously studied by Haupt and Lion[54]. The constitutive relation is described as

$$\boldsymbol{\sigma} = \mu_{\alpha}\mathbf{F}D^{\alpha}\left(\mathbf{I} - \mathbf{F}^{-1}\mathbf{F}^{-T}\right)\mathbf{F}^T - p_0\mathbf{I}, \tag{22}$$

where $\mu_{\alpha} = G_0\tau_0^{\alpha}$ is a viscoelastic shear modulus with a unit of $\mathrm{Pa}\cdot\mathrm{s}^{\alpha}$. By considering the $\alpha = 0$ and $\alpha = 1$ cases, we see that the fractional viscoelastic material transitions between a Neo-Hookean solid and Newtonian fluid:

$$\begin{aligned}
&\boldsymbol{\sigma} = \mu_{\alpha}\mathbf{F}\mathbf{F}^T - p_1\mathbf{I} \qquad (\alpha = 0,\ \text{elastic solid}) \\
&\boldsymbol{\sigma} = 2\mu_{\alpha}\mathbf{D} - p_2\mathbf{I} \qquad (\alpha = 1,\ \text{Newtonian fluid}).
\end{aligned} \tag{23}$$

It can be seen that the viscoelastic modulus becomes an elastic modulus at the purely elastic extreme—i.e., $\mu_{\alpha=0} = G_e$. At the purely viscous extreme, the viscoelastic modulus becomes a viscous modulus—i.e., $\mu_{\alpha=1} = G_0\tau_0 = \mu_v$. Therefore, the viscoelastic modulus can also be viewed as a quantity that transitions between G_e and μ_v as the material behavior transitions between pure elasticity and pure viscosity.

For the inertial cavitation problem considered in the present study, the non-zero components of the deviatoric Cauchy stress can be evaluated for a fractional viscoelastic material:

$$\begin{aligned}
s_{\theta\theta}^{neq} = -\frac{s_{rr}^{neq}}{2} = &\frac{\mu_{\alpha}}{3}\left[D^{\alpha}(1)\left(\lambda^2 - \lambda^{-4}\right)\right. \\
&\left. + D^{\alpha}\left(\lambda^4\right)\lambda^{-4} - D^{\alpha}\left(\lambda^{-2}\right)\lambda^2\right]
\end{aligned} \tag{24}$$

in which the term $D^{\alpha}(1)$ is equal to zero when the material is non-elastic—i.e., $\alpha \neq 0$. For brevity, we neglect the purely

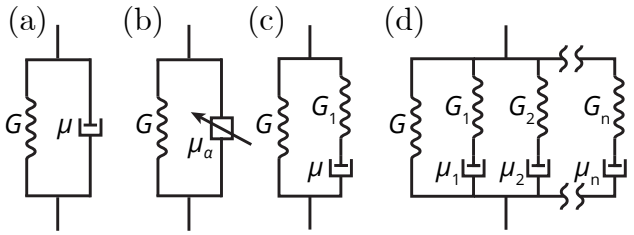

FIG. 2. Spring and dashpot models of viscoelastic materials investigated in this work, including (a) Kelvin-Voigt, (b) Fractional Kelvin-Voigt, (c) Standard Non-linear solid, and the (d) Generalized Maxwell models.

elastic case and evaluate the stress integral for cases in which $0 < \alpha \leq 1$:

$$S^{neq} = \mu_\alpha \int_R^\infty \frac{1}{r(t)} \left[D^\alpha \left(\lambda^{-2}\right) \lambda^2 - D^\alpha \left(\lambda^4\right) \lambda^{-4} \right] dr \tag{25}$$

The numerical evaluation of the stress integral is discussed further in the Numerical Methods section.

The stress integral expression for the ground-state Neo-Hookean, Newtonian, Maxwell, and springpot responses, developed above, are summarized in Table 1.

2. *Bubble internal pressure*

Following previous works[38,39], we treat the bubble contents as a mixture of water vapor and non-condensible gas in a homobaric state and assume they follow the ideal gas law.

The mass diffusion of the bubble contents is assumed to obey Fick's law, i.e.:

$$j_v = -j_g = -\rho_m D \frac{\partial k}{\partial r}, \tag{26}$$

where j_v and j_g are the radial mass fluxes of the water vapor and non-condensible gas, respectively; ρ_m is the density of the mixture; D is a constant binary diffusion coefficient; and $k = \rho_v/\rho_m$ is the mass fraction of the vapor.

The heat transfer of the bubble contents is assumed to obey Fourier's law, i.e.:

$$\begin{aligned} &\rho_m \left[k \left(\frac{\partial h_v}{\partial t} + v_m \frac{\partial h_v}{\partial r} \right) + (1-k) \left(\frac{\partial h_g}{\partial t} + v_m \frac{\partial h_g}{\partial r} \right) \right] \\ &\quad = \dot{p}_b + \frac{1}{r^2} \frac{\partial}{\partial r} \left(r^2 K \frac{\partial T}{\partial r} \right) - j_v \frac{\partial}{\partial r} \left(h_v - h_g \right), \end{aligned} \tag{27}$$

where h_v and h_g are the specific enthalpies of the water vapor and non-condensible gas; $v_m(r,t)$ is the radial mixture velocity; $T(r,t)$ is the temperature, which is assumed to be equal between the water vapor and non-condensible gas for a given radial coordinate r and time t; and $K(T) = AT + B$ is the thermal conductivity of the mixture, which is assumed to scale linearly with temperature, following the approach of Prosperetti et al.[5].

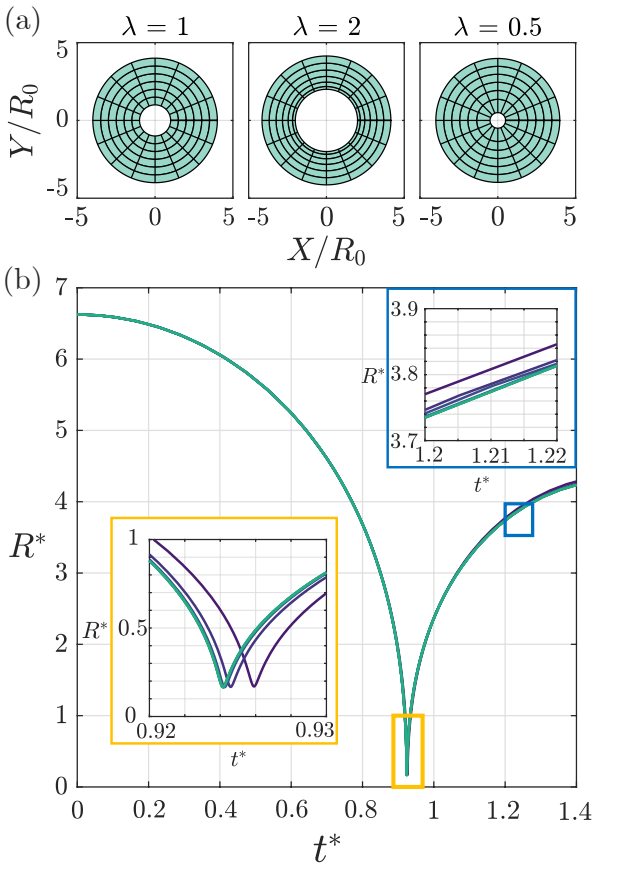

FIG. 3. (a) Illustration of spatial mesh deformation during cavitation, with numerical integration error increasing during bubble collapse due to elongated mesh. (b) Illustration of convergence for the numerical solution over different spatial mesh densities for $\mu_\alpha = 1.0\text{Pa}\cdot\text{s}^\alpha$, $\alpha = 0.7$. From dark purple to light green, the number of elements in the mesh varies from 75 to 8553, with 8 total increments. The selected mesh with 2145 nodes was sufficient to within 0.1% error for spatial integration using trapezoidal method.

B. Numerical Methods

1. *Non-dimensionalization*

To obtain a generalized description of the cavitation process and clarify the interactions between material parameters, we perform non-dimensionalization of the governing equations as in prior work[38,39]. The system is non-dimensionalized using the maximum bubble radius $R_{\max}$, the far-field pressure p_∞, the surrounding material density ρ, and the far-field temperature T_∞. A characteristic velocity $v_c = \sqrt{p_\infty/\rho}$ is defined accordingly, allowing for dimensionless quantities to be constructed as summarized in Table 2. The dimensionless Keller-Miksis equation describing the evolution of the dimensionless

TABLE 1. Stress integral due to different material models.

Material model	Parameters	Stress Integral, S
Neo-Hookean	G	$\frac{G}{2}\left[\left(\frac{R_0}{R}\right)^4+4\frac{R_0}{R}-5\right]$
Newtonian	μ	$\frac{-4\mu\dot{R}}{R}$
Maxwell	μ, $G_1=\mu/\tau_1$	$-12G_1\int_R^\infty \frac{1}{r(t)}\left[\int_{-\infty}^t e^{(z-t)/\tau_1}\frac{v(z)}{r(z)}dz\right]dr$
Springpot	μ_α, α	$\mu_\alpha\int_R^\infty \frac{1}{r(t)}\left[D^\alpha\left(\lambda^{-2}\right)\lambda^2-D^\alpha\left(\lambda^4\right)\lambda^{-4}dr\right]$

bubble radius $R^*(t^*)$ is:

$$\begin{aligned}\left(1-\frac{\dot{R}^*}{c^*}\right)R^*\ddot{R}^*+\frac{3}{2}\left(1-\frac{\dot{R}^*}{3c^*}\right)\dot{R}^{*2}\\ =\left(1+\frac{\dot{R}^*}{c^*}\right)\left(p_b^*-\frac{1}{\mathrm{We}R^*}+S^*-1\right)\\ +\frac{R^*}{c^*}\dot{\overline{\left(p_b^*-\frac{1}{\mathrm{We}R^*}+S^*\right)}}\end{aligned} \tag{28}$$

2. Integral Evaluation

Given that the history of bubble radius is evaluated numerically, numerical integration must be performed both spatially and temporally to evaluate the stress integral term S when the Maxwell and springpot viscoelastic models are used.

For the Maxwell model, Equation 20 may be rewritten as

$$\begin{aligned}S&=-12G_1\int_R^\infty\frac{1}{r(r_0,t)}q(r_0,t)dr,\\ q(r_0,t)&=\int_{-\infty}^t e^{(s-t)/\tau_1}\frac{v_r(r_0,s)}{r(r_0,s)}ds.\end{aligned} \tag{29}$$

Assuming a temporal increment of Δt between two consecutive time steps, the updated value of $q(r_0,t+\Delta t)$ is

$$\begin{aligned}q(r_0,t+\Delta t)&=\int_{-\infty}^{t+\Delta t}e^{(s-t-\Delta t)/\tau_1}\frac{v_r(r_0,s)}{r(r_0,s)}ds\\ &=q(r_0,t)e^{-\Delta t/\tau_1}+\int_t^{t+\Delta t}e^{(s-t-\Delta t)/\tau_1}\frac{v_r(r_0,s)}{r(r_0,s)}ds.\end{aligned} \tag{30}$$

For the purpose of numerical integration, only the most recent value of $q(r_0,t)$ needs to be tracked. The computational cost of the time integration for the Maxwell model does not increase with the duration of cavitation history simulated.

For the fractional viscoelastic model, Equation 25 is numerically integrated to evaluate the stress integral. In particular, the fractional derivative functions, corresponding to gradual relaxation of stress, are evaluated through numerical time integration. Here, we evaluate the fractional derivative of a function $y(t)$ over non-uniform time steps according to a procedure introduced by Zhang et al.[55]:

$$\begin{aligned}D^\alpha(y)&=\frac{1}{\Gamma(1-\alpha)}\int_{-\infty}^t\frac{dy}{ds}(t-s)^{-\alpha}ds\\ &\approx\frac{1}{\Gamma(2-\alpha)}\sum_{k=1}^n\dot{y}_k\Psi_k\end{aligned} \tag{31}$$

$$\Psi_k=\left[(t-t_{k-1})^{1-\alpha}-(t-t_k)^{1-\alpha}\right] \tag{32}$$

in which the property $\Gamma(x+1)=x\cdot\Gamma(x)$ is used. Correspondingly, the stress integral for the fractional viscoelastic model is rewritten in its approximate form as

$$\begin{aligned}S\approx\frac{\mu_\alpha}{\Gamma(2-\alpha)}\int_R^\infty\frac{1}{r(r_0,t)}\\ \left[\lambda^2(r_0,t)\left(\sum_{k=1}^n\Psi_k\dot{\overline{\lambda^2}}\right)-\lambda^{-4}(r_0,t)\left(\sum_{k=1}^n\Psi_k\dot{\overline{\lambda^{-4}}}\right)\right]dr\end{aligned} \tag{33}$$

Evaluation of Ψ_k must be performed for all $k\in[1,n]$ at the n-th temporal step. As a result, the computational cost of the time integration of models incorporating fractional elements increases with the number of temporal steps taken.

For the non-dimensionalized form of the Keller-Miksis equation, we define a dimensionless fractional modulus and name it the *Zener number*:

$$\mathrm{Ze}=\frac{p_\infty^{1-\alpha/2}\rho^{\alpha/2}R_{\max}^\alpha}{\mu_\alpha} \tag{34}$$

For the cases where $\alpha=0$ and 1, the Zener number is equivalent to the Cauchy number and Reynolds number, respectively.

Since the stress integral is evaluated across the deformed radial coordinate $r(r_0)$, a spatial mesh of r_0 must be selected such that the evaluation of Equations 29 and 33 remains accurate for the typical range of λ and $\dot{\lambda}$ observed in IMR. As illustrated in Figure 3, the spacing between consecutive spatial nodes increases when the cavitated bubble collapses. We note that, due to spherical symmetry, we need only refine the mesh in 1D; Figure 3 shows a 2D representation for ease of visualization. For the trapezoidal method, the numerical integration of a twice-continuously differential function $f(r)$ across a single spatial mesh between $r=r_a$ and $r=r_b$ has the error[56]

$$\int_{r_a}^{r_b}f(r)dr-T(f(r))=-\frac{f''(r_c)}{12}h^3=\varepsilon\int_{r_a}^{r_b}f(r)dr \tag{35}$$

TABLE 2. Dimensionless quantities.

Dimensional quantity	Dimensionless quantity	Name
t	$t^* = tv_c/R_{\max}$	Time
R	$R^* = R/R_{\max}$	Bubble-wall radius
R_0	$R_0^* = R_0/R_{\max}$	Equilibrium bubble-wall radius
c	$c^* = c/v_c$	Material wave speed
p_b	$p_b^* = p_b/p_\infty$	Bubble pressure
γ	$\mathrm{We} = p_\infty R_{\max}/(2\gamma)$	Weber number
S	$S^* = S/p_\infty$	Stress integral
G	$\mathrm{Ca} = p_\infty/G$	Cauchy number
μ	$\mathrm{Re} = \rho v_c R_{\max}/\mu$	Reynolds number
G_1/μ	$\mathrm{De} = \mu v_c/(G_1 R_{\max})$	Deborah number
μ_α	$\mathrm{Ze} = p_\infty^{1-\alpha/2}\rho^{\alpha/2}R_{\max}^\alpha/\mu_\alpha$	Zener number
D	$\mathrm{Fo} = D/(v_c R_{\max})$	Mass Fourier number
T	$T^* = T/T_\infty$	Temperature
K	$K^* = K/K(T_\infty)$	Mixture thermal conductivity
$K(T_\infty)T_\infty$	$\chi = K(T_\infty)T_\infty/(p_\infty v_c R_{\max})$	Lockhart-Martinelli number
$p_{v,sat}(T_\infty)$	$p_{v,sat}^* = p_{v,sat}(T_\infty)/p_\infty$	Vapor saturation pressure

where $r_c \in [r_a, r_b]$, $h = r_b - r_a$ is the mesh size, and $T(f(r))$ is the numerical approximation. Accordingly, the spatial mesh size at coordinate r must satisfy

$$h(r) = \sqrt{12\varepsilon_0 f(r)/f''(r)} \tag{36}$$

to achieve an overall numerical error of $\varepsilon \approx \varepsilon_0$. In the present study, a spatial mesh of $r_0 \in [R_0, 100\ R_0]$ with 2,145 nodes is selected so that $\varepsilon_0 = 10^{-3}$ is enforced for both the integrands in Equations 7 and 11 (i.e., the purely elastic and viscous extreme cases) when $R/R_0 > 0.1$.

C. Experiments

The working principle of the microcavitation experiments follows the spirit of that introduced by Estrada et al.[38], with three main advancements of (1) split-view imaging (green), (2) shadowgraphy and ghost imaging (blue), and (3) incident beam shaping, as shown in Figure 4. During each experiment, a single microcavitation bubble was generated via one pulse of a user-adjustable 1–50 mJ, frequency-doubled Q-switched 532 nm Nd:YAG laser (Continuum, San Jose, CA). Single-sensor, two-perspective imaging was performed at approximately 1 million frames per second (Mfps) using a Shimazdu HPV-X2 (Tokyo, Japan). By illuminating and imaging the laser-induced-cavitation bubble dynamics with two orthogonal imaging paths, we ensure the setup is generating spherically symmetric bubbles. The use of a spatial light modulator(SLM) (Holoeye, Berlin, German) allows for higher control over the last pulse shape and energy.[57]

Using our own custom Inertial Cavitation Acquisition (InCA) software, collected images from the axial and transverse perspectives can be separately analyzed for bubble kinematics. For the present study, the average spherical radii over time were used to perform viscoelastic model calibration.

To measure the wave speed in the medium, we deployed two imaging techniques simultaneously: laser shadowgraphy[58] and ghost-imaging[59]. Shadowgraphy (a form of Schlieren) imaging is performed by manipulating the backlighting path to capture variation in density due the compressive shockwave, allowing us to capture the physical location of the pressure wave during cavitation and collapse of the bubble. Ghost imaging is achieved by triggering the strobed backlight a user-defined number of times per camera exposure, usually 2 or 3 per frame.

Polyacrylamide gels for characterization purposes were prepared at a concentration of 10/0.06% acrylamide/bisacrylamide according to previously developed protocols[38,60]. The polyacrylamide gels were cast in square 5mL polystyrene spectrophotometer cuvettes and cured for 45 minutes.

III. REDUCED-ORDER MODELING

In our previous work[38], viscoelastic model calibration was achieved by sweeping over a realistic range of parametric values and evaluating the least-squares error between the bubble deformation history in each simulation and the experimental data. This procedure becomes cost prohibitive as the total number of parameters increases for advanced viscoelastic models reflecting complex time-dependent behaviors. Therefore, it is beneficial to (a) decrease the total number of material parameters that require calibration and (b) reduce the range of parameteric values in which sweeping is performed. The former motivates the use of a constitutive model such as the fractional viscoelastic springpot, which captures power-law stress relaxation with much fewer parameters than the generalized Maxwell framework. The latter can be achieved by developing a physics-based reduced-order model for the bubble radius evolution, which would produce an initial estimate of the viscoelastic model parameter values. In this section, we present such a reduced-order procedure, which will be referred to as RO-IMR from here onward.

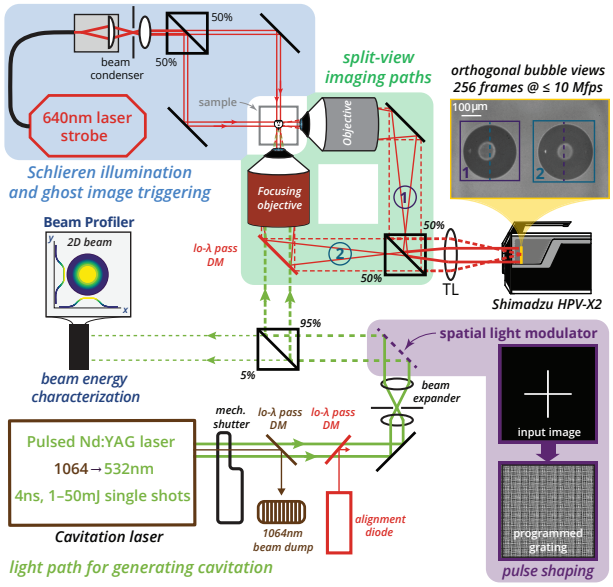

FIG. 4. The experimental setup generates, records, and profiles single laser-induced microcavitation (LIC) bubble events in soft hydrogels and materials using a combination of a class-4, frequency-doubled Q-switched 532 nm Nd:YAG pulsed laser, high speed imaging camera and a spatial light modulator.

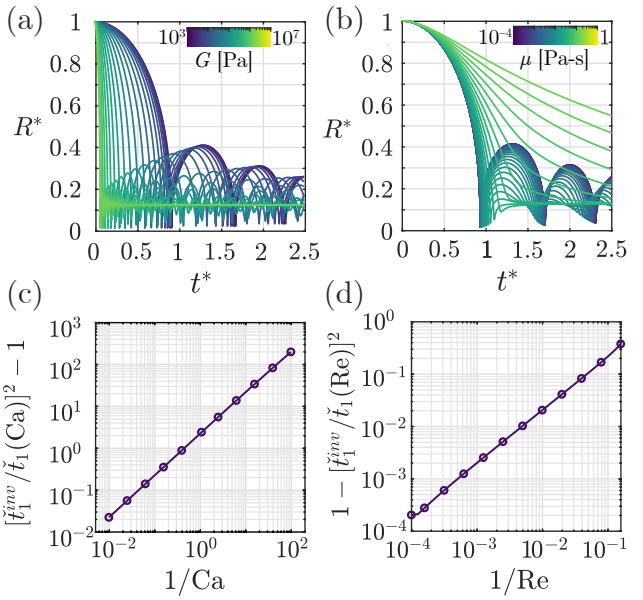

FIG. 5. Time history of bubble evolution for a (a) Neo-Hookean model with elastic modulus ranging from 10^3 (Ca = 100) to 10^7 Pa (Ca = 0.01) and (b) Newtonian model with viscous modulus ranging from 10^{-4} (Re = 10^4) to 1 Pa s (Re = 1). Scaling of initial collapse time $\check{t}_1$ for the corresponding (c) Neo-Hookean and (d) Newtonian materials.

A. Effect of elasticity, viscosity, and viscoelasticity on initial collapse duration

First, we consider the inertial cavitation in a Neo-Hookean elastic solid. By re-arranging the Keller-Miksis equation (i.e., Equation 1), we can express the instantaneous acceleration of the bubble wall as

$$\ddot{R} = \frac{1}{\left(1-\frac{\dot{R}}{c}\right)R}\left[\frac{1}{\rho}\left(1+\frac{\dot{R}}{c}\right)\left(p_b - \frac{2\gamma}{R} + S - p_\infty\right) + \frac{1}{\rho}\frac{R}{c}\frac{\dot{}}{}\left(p_b - \frac{2\gamma}{R} + S\right) - \frac{3}{2}\left(1-\frac{\dot{R}}{3c}\right)\dot{R}^2\right] \tag{37}$$

in which only S and $\dot{S}$ depend on the elastic modulus G, as shown in Equation 7. Accordingly, we propose a linearized approximation of the form

$$\frac{\ddot{R}(G)}{\ddot{R}^{inv}} = 1 + \frac{G}{G_0} \tag{38}$$

where $\ddot{R}^{inv}$ is the acceleration when the cavitating medium is inviscid ($G = 0$) and G_0 is a scaling parameter.

We denote the time elapsed between when the bubble wall reaches the maximum radius of $R_{\max}$ and when it decelerates to a velocity of zero as the initial collapse time $\check{t}_1$. We surmise that the collapse process is analogous to the dynamic motion of a simple gravity pendulum with length scale l subjected to acceleration g. The pendulum completes a cycle of swinging over a time period of $T \approx 2\pi\sqrt{l/g}$. Assuming accordingly that $\check{t}_1 \propto 1/\sqrt{\ddot{R}(G)}$ for the collapsing bubble, an approximate scaling law for the initial collapse time is proposed as

$$\check{t}_1(G) = \check{t}_1^{inv}\left(1+\frac{G}{G_0}\right)^{-1/2} \tag{39}$$

where $\check{t}_1^{inv}$ is the initial collapse time in an inviscid material.

To validate the scaling law, simulations were performed for cavitation in a Neo-Hookean elastic material with elastic modulus G ranging from 10^3 to 10^7Pa with $R_{\max} = 100\,\mu$m. The time history is shown in Figure 5a, indicating a monotonic decrease of $\check{t}_1(G)$ following the increase of G. The linear relation between $\sqrt{\check{t}_1^{inv}/\check{t}_1(G)} - 1$ and G shown in Figure 5c confirms the effectiveness of the proposed scaling law.

Similarly, we propose a scaling law for the initial collapse time in Newtonian viscous fluid:

$$\check{t}_1(\mu) = \check{t}_1^{inv}\left(1-\frac{\mu}{\mu_0}\right)^{-1/2} \tag{40}$$

Here, the addition of viscosity dampens the system and extends the initial collapse time. The validity of the scaling is confirmed in Figure 5. We further extend the scaling law to the cases of the Maxwell and the fractional viscoelastic models. Given a constant relaxation parameter, τ_1 or α, we expect the initial collapse time $\check{t}_1$ to follow the relation

$$\check{t}_1(\mu,\tau_1) = \check{t}_1^{inv}\left(1-\frac{\mu}{\mu_0}\right)^{-1/2} \quad \text{(Maxwell model)} \tag{41}$$

$$\check{t}_1(\mu_\alpha,\alpha) = \check{t}_1^{inv}\left(1-\frac{\mu_\alpha}{\mu_{\alpha 0}}\right)^{-1/2} \quad \text{(Springpot model)} \tag{42}$$

For the case of the fractional viscoelastic model, the transition of α from 1 to 0 corresponds to a transition from a Newtonian fluid to a Neo-Hookean solid. As shown in Fig. 7, a springpot model with a large α will slow down the initial collapse process and increase $\check{t}_1$ with increasing μ_α, similar to a Newtonian model. A springpot model with a small α will speed up the initial collapse process and decrease $\check{t}_1$ with increasing μ_α, similar to a Neo-Hookean model. In Equation 42, the scaling parameter $\mu_{\alpha 0}$ will be a positive value for a large α and a negative value for small α.

It should be noted, however, that the proposed scaling law for $\check{t}_1$ is only effective for materials with a low to moderate level of viscosity. In the case of a Newtonian fluid, as seen in Figure 5, high viscosity leads to overdamping of the dynamic system. As a result, the bubble wall radius no longer oscillates over time but instead gradually relax from $R_{\max}$ to R_{eq}. For the Maxwell viscoelastic model, the fading memory of the material contributes to a more complex time-dependent response. It is observed that the deviation from the scaling law generally occurs at Re < 10. For cavitation experiments with $R_{\max} \approx 100\ \mu$m, this imposes an upper bound of $\mu \approx 0.10$ Pa·s for accurate reduced-order calibration of Maxwell models. This upper bound for μ increases linearly with $R_{\max}$ of the performed experiment.

For a Kelvin-Voigt framework, we expect the combined effect of the material parameters to be multiplicative, i.e.

$$\check{t}_1(G,\mu) = \check{t}_1^{inv}\left(1+\frac{G}{G_0}\right)^{-1/2}\left(1-\frac{\mu}{\mu_0}\right)^{-1/2}. \tag{43}$$

B. Model calibration according to initial collapse time

The non-dimensionalized parameters summarized in Table 2 show that the dimensionless elasticity of the system Ca $= p_\infty/G$ is independent of the bubble size scale $R_{\max}$, while the dimensionless viscosity Re scales with $R_{\max}$ when μ is held constant. That is, the same material displays stronger viscous effects (i.e., lower Re) when the cavitating bubble is smaller, causing the dimensionless governing equation 28 to evolve differently. Taking advantage of this effect, a Kelvin-Voigt model, consisting of a Neo-Hookean spring and a Newtonian dashpot in parallel, can be calibrated according to experiments performed at two different length scales $R^A_{\max}$ and $R^B_{\max}$.

$$\begin{aligned}\left(1+\frac{G}{G_0^A}\right)\left(1-\frac{\mu}{\mu_0^A}\right) &= \left(\frac{\check{t}_1^{A,inv}}{\check{t}_1^A}\right)^2 \\ \left(1+\frac{G}{G_0^B}\right)\left(1-\frac{\mu}{\mu_0^B}\right) &= \left(\frac{\check{t}_1^{B,inv}}{\check{t}_1^B}\right)^2\end{aligned} \tag{44}$$

The exact solution to this pair of equations is

$$\begin{aligned}G &= \frac{\pm a + b - c_A + c_B}{2(\mu_0^A - \mu_0^B)} \\ \mu &= \frac{\pm a + b + c_A - c_B}{2(G_0^A - G_0^B)}\end{aligned} \tag{45}$$

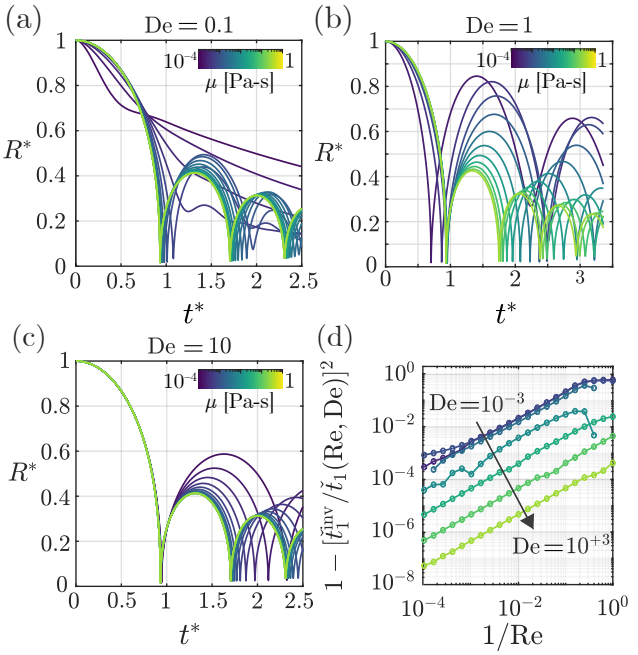

FIG. 6. Time history of bubble evolution for Maxwell models with viscous modulus ranging from 10^{-4} (Re $= 10^4$) to 1 Pa·s (Re $= 1$) and relaxation time scales of (a) $\tau = 10^{-6}$ s (De $= 0.1$), (b) $\tau = 10^{-5}$ s (De $= 1$), and (c) $\tau = 10^{-4}$ s (De $= 10$). (d) Scaling of initial collapse time $\check{t}_1$ with the viscous modulus for Maxwell models with De ranging from 10^{-3} to 10^3.

where

$$\begin{aligned}a &= \Big[\left(-G_0^A\mu_0^B + G_0^B\mu_0^A + c_A - c_B\right)^2 \\ &\quad - 4\left(\mu_0^A - \mu_0^B\right)\left(G_0^B c_A - G_0^A c_B\right)\Big]^{1/2} \\ b &= G_0^A\mu_0^B - G_0^B\mu_0^A \\ c_A &= G_0^A\mu_0^A\left[1-\left(\frac{\check{t}_1^{A,inv}}{\check{t}_1^A}\right)^2\right] \\ c_B &= G_0^B\mu_0^B\left[1-\left(\frac{\check{t}_1^{B,inv}}{\check{t}_1^B}\right)^2\right].\end{aligned}$$

This results in two sets of solutions. Only one set of solution corresponds to realistic, positive values of G and μ. Therefore, an approximation of G and μ can be achieved with inertial cavitation experiments at two length scales, $R^A_{\max}$ and $R^B_{\max}$, and three numerical simulations of the bubble dynamics at each scale to retrieve the values of $\check{t}_1^{inv}$, G_0, and μ_0.

For the standard nonlinear solid and fractional Kelvin-Voigt viscoelastic models, the third parameter—i.e., τ_1 for the Maxwell element and α for the springpot—is identified through a manual refinement process. Specifically, the rate-dependent element in the generalized Kelvin-Voigt model will be perturbed from the pure Newtonian fluid case by increasing τ_1 for the Maxwell case or $(1-\alpha)$ for the springpot case from the Newtonian limit value of 0. According to the oscillation behaviors demonstrated in the RO-calibrated model, the third

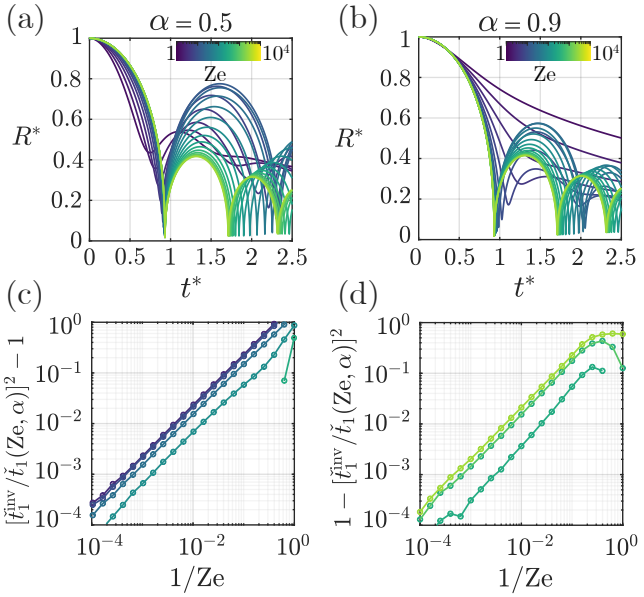

FIG. 7. Time history of bubble evolution for fractional viscoelastic springpot models with nondimensional modulus Ze ranging from 1 to 10^4 and α values of (a) 0.5 and (b) 0.9. (c) Scaling of initial collapse time $\check{t}_1$ with Ze for springpot models with α ranging from 0.01 to 0.5. (d) Scaling of initial collapse time $\check{t}_1$ with Ze for springpot models with α ranging from 0.7 to 0.99.

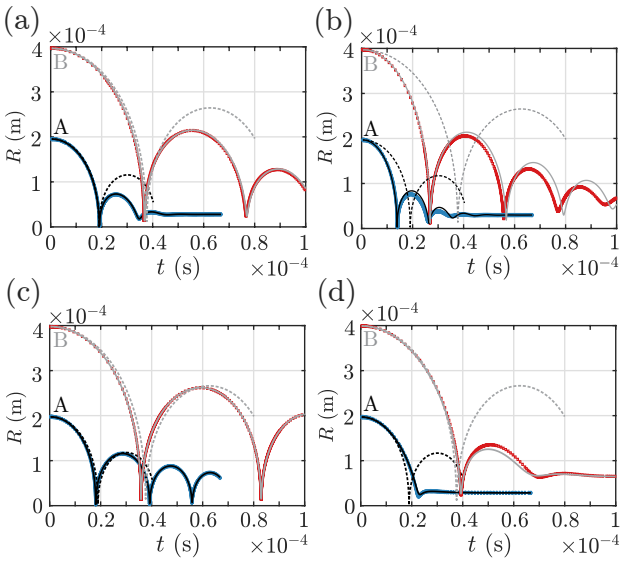

FIG. 8. Reproduction of simulated bubble dynamics for Kelvin-Voigt viscoelastic materials: effect of G and μ on RO approximation. (a) Case 1: $G = 4.8\,\text{kPa}$, $\mu = 0.109\,\text{Pa s}$; (b) Case 3: $G = 48\,\text{kPa}$, $\mu = 0.109\,\text{Pa s}$; (c) Case 4: $G = 4.8\,\text{kPa}$, $\mu = 0.001\,09\,\text{Pa s}$; (d) Case 5: $G = 4.8\,\text{kPa}$, $\mu = 0.327\,\text{Pa s}$. Blue circles denote the target bubble dynamics for length scale A and red squares denote the target bubble dynamics for length scale B. The solid curves are the bubble dynamics of the consitutive model calibrated from RO-IMR. The dashed curves correspond to the bubble dynamics of inviscid fluid at the two length scales.

parameter is refined over a small number of iterations until the possible range of the parametric value is narrowed down to a sufficiently small range.

The effectiveness of the proposed scaling law and RO calibration procedure is verified in the Results section through inverse characterization of simulation and experiment data.

C. Shadowgraph imaging

Due to the high deformation rate immediately before and after $\check{t}_1$, a shockwave is formed at the bubble wall and propagates toward the far-field. The emission of shockwaves during bubble collapse has been reported previously in laser-induced cavitation experiments[61–63]. Based on the relative position between the traveling shock front and the rebounding bubble wall, as captured by the shadowgraphy system in the first frame after $\check{t}_1$ at time $\check{t}_1 + \Delta t_s$, we can estimate the distance traveled by the shock wave during Δt_s and accordingly estimate Δt_s. This allows for $\check{t}_1$ to be estimated at a level of precision finer than the camera frame rate and, as a result, drastically reduces error from the experimental quantification of the collapse time. We discuss this further in the following section.

IV. RESULTS

A. Reproduction of IMR simulation

To verify the effectiveness of the proposed RO calibration approach, we select arbitrary sets of viscoelastic material parameters within the ranges of our common material behavior, perform simulation of the corresponding cavitation process at two scales of R_{max}, and then apply the RO framework to estimate the input material parameters. Given that the target cavitation process is computationally generated, the RO-IMR procedure should ideally reproduce the input material parameters and the corresponding bubble dynamics.

First, we examine the finite deformation Kelvin-Voigt model using combinations of input parameters as summarized in Table 3. The results for Cases 1 through 5 are presented in Figure 8. The parameters used in Case 1 reflect the typical range of bubble size achieved in IMR experiments and the typical magnitude of material moduli measured in soft biological tissues. At this scale, the RO-IMR procedure is capable of reproducing the viscoelastic model within small errors of 0.30% and 2.7% for G and μ, respectively. In Case 2, an elastic modulus of $G = 48.0\,\text{Pa}$ is used. In this case, the influence of G is significantly lower and much more challenging to capture with the RO-IMR procedure. Consequentially, the error of the G estimation is over 140%, while the error of the μ estimation is only 3.2%. Similarly, when the viscous modulus μ is set to a low value for Case 4, the viscous contribution is difficult to discern. However, for both Cases 2 and 4, the time histories of the bubble radius are reproduced accurately, since the error in material moduli do not contribute significantly to the bubble dynamics.

For Case 3, a high value of G was considered. The proposed scaling law relating $\check{t}_1$ to G is less effective when the

TABLE 3. Input parameters and estimated viscoelastic moduli of simulation reproduction cases for Kelvin-Voigt model.

Case	$R^A_{\max}$ [μm]	$R^B_{\max}$ [μm]	G [Pa]	μ_α [Pa s]	Estimated G [Pa]	Estimated μ [Pa s]
1	200	400	4.800×10^{3}	1.090×10^{-1}	4.814×10^{3}	1.060×10^{-1}
2	200	400	4.800×10^{1}	1.090×10^{-1}	1.158×10^{2}	1.112×10^{-1}
3	200	400	4.800×10^{4}	1.090×10^{-1}	4.814×10^{3}	7.642×10^{-2}
4	200	400	4.800×10^{3}	1.090×10^{-3}	4.780×10^{3}	7.161×10^{-4}
5	200	400	4.800×10^{3}	3.270×10^{-1}	6.199×10^{3}	3.662×10^{-1}
6	100	500	4.800×10^{3}	1.090×10^{-1}	4.947×10^{3}	1.114×10^{-1}
7	250	300	4.800×10^{3}	1.090×10^{-1}	4.859×10^{3}	1.069×10^{-1}

modulus is high. As a result, the RO-IMR procedure not only underestimates μ by an error of 29.9%, but is also unable to reproduce the bubble dynamics accurately. Similar results are observed in Case 5, where a high value of μ was considered. As the smaller size scale tested, the bubble oscillation is effectively suppressed after the first cycle due to the high viscosity. Here, G and μ are over-estimated by RO with errors of 29.1% and 12.0%, respectively.

Figure 9 compares the bubble dynamics simulated for Cases 1, 6, and 7, for which the viscoelastic parameters G and μ are the same but the pairings of $R_{\max}$ differ. No significant differences can be observed in the performance of the RO-IMR procedure for these cases. However, this is due to the fact that an exact value of $\check{t}_1$ is obtained from each target simulation and used to calibrate the viscoelastic model. In typical experimental characterization of materials with IMR, the accuracy of $\check{t}_1$ measured is limited by factors including camera frame rate and noise in collected data. To illustrate this effect, we re-run Cases 1, 6, and 7 but with perturbed input values for the collapse times. The collapse time $\check{t}^A_1$ for the smaller length scale is increased by 1% while the collapse time $\check{t}^B_1$ for the larger length scale is lower by 1%. In this case, the combination of $R^A_{\max}=200\,\mu$m and $R^B_{\max}=400\,\mu$m (Case 1) estimates the viscoelastic parameters to be $G=7.65\,$kPa and $\mu=0.166\,$Pa s, the combination of $R^A_{\max}=100\,\mu$m and $R^B_{\max}=500\,\mu$m (Case 6) estimates the viscoelastic parameters to be $G=6.37\,$kPa and $\mu=0.128\,$Pa s, and the combination of $R^A_{\max}=250\,\mu$m and $R^B_{\max}=300\,\mu$m (Case 7) estimates the viscoelastic parameters to be $G=15.20\,$kPa and $\mu=0.304\,$Pa second. By comparing the predicted bubble dynamics shown in Figure 9, the advantage of having a large difference between $R^A_{\max}$ and $R^B_{\max}$ becomes even clearer.

To further illustrate the effect of collapse time measurement error on the performance of the RO calibration procedure, the expected error of (G,μ) estimated from various combinations of errors in $\check{t}^A_1$ and $\check{t}^B_1$ ranging between $\pm1\%$ is calculated according to Equation 45 and shown in Figure 10. When the difference between $R^A_{\max}$ and $R^B_{\max}$ are larger, the RO-IMR procedure is more resilient to error in the measurement of collapse time. When $R^A_{\max}$ and $R^B_{\max}$ are too close to each other, an error less than 1% in the collapse time measurement may lead to no physical solution for the system according to the RO-IMR procedure.

Next, we perform an iterative solution to reproduce the simulated bubble dynamics of an example standard nonlinear solid material with parameteric values of $G=4.8\,$kPa, $\mu=0.109\,$Pa s, and $\tau_1=2.5\times10^{-6}\,$s. The relaxation time scale is assumed to be 0 during the initial iteration, corresponding to the Maxwell element behaving as a Newtonian fluid. Due to the fading memory effect of the Maxwell element, the standard linear model typically exhibits a higher peak radius during the second oscillation cycle, $\hat{R}_2$ as compared to a Kelvin-Voigt model with similar behavior during the initial collapse. Within a moderate range of τ_1, the amplitude of $\hat{R}_2$ increases monotonically with τ_1. Therefore, if the simulated bubble dynamics underestimates $\hat{R}_2$ during a previous RO iteration, the relaxation time scale is increased during the succeeding iteration. On the contrary, if $\hat{R}_2$ is overestimated during a previous iteration, the relaxation time scale is decreased during the next iteration. An accurate estimate of τ_1 is thereby achieved by gradually narrowing down the range of possible values across multiple iterations, as shown in Figure 11. As shown in Table 4, the estimated values of viscoelastic parameters also converge to the target values following additional iterations.

To further evaluate the goodness-of-fit achieved by the iterative solution process, the least-squares error is evaluated between the target and estimated bubble dynamics. The error measure is defined as

$$e=\sum_{k=1}^{n}\left(\tilde{t}^*_k-t^*_k\right)^2+\left(\tilde{R}^*_k-R^*_k\right)^2 \tag{46}$$

where $t^*_k=t_k/t_c$ and $R^*_k=R_k/R_{\max}$ are the normalized time and radius at the k-th experimental measurement and $(\tilde{t}^*_k,\tilde{R}^*_k)$ is a point on the simulated bubble dynamics curve that is closest to (t^*_k,R^*_k). For the present study, the least-squares error is evaluated between the first three peaks of the bubble oscillation, such that $t_1=0$ and t_n corresponds to the end of the second rebound. As the relaxation time scale τ_1 converges toward the target value through iterations, the least-squares error of the bubble dynamics also decreases.

A similar example case is conducted for the fractional Kelvin-Voigt model, with target parameters of $G=4.8$ kPa, $\mu_\alpha=0.327$ Pa$\cdot$s$^\alpha$, and $\alpha=0.86$. Similar to the iteration procedure for the standard nonlinear solid model, an initial iteration is performed assuming $\alpha=1$, corresponding to a

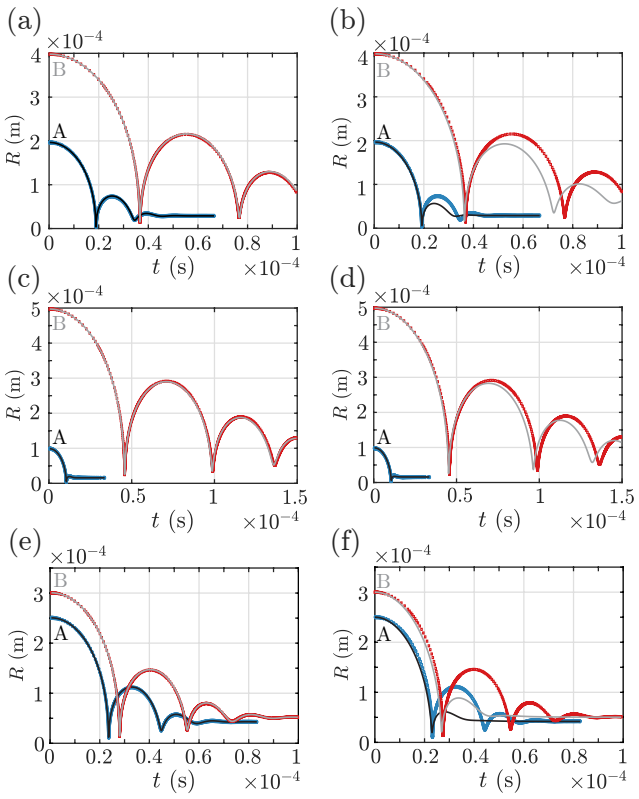

FIG. 9. Reproduction of simulated bubble dynamics for Kelvin-Voigt viscoelastic materials: effect of $\check{t}_1$ estimation error on performance of RO-IMR. (a) $R_A = 200\,\mu$m and $R_B = 400\,\mu$m, exact input of $\check{t}_1$ (Case 1) and (b) input of $\check{t}_1$ with 1% error; (c) $R_A = 100\,\mu$m m and $R_B = 500\,\mu$m m, exact input of $\check{t}_1$ (Case 6) and (d) input of $\check{t}_1$ with 1% error; (e) $R_A = 250\,\mu$m and $R_B = 300\,\mu$m m, exact input of $\check{t}_1$ (Case 7) and (f) input of $\check{t}_1$ with 1% error. Blue circles denote the target bubble dynamics for length scale A and red squares denote the target bubble dynamics for length scale B. The solid curves are the bubble dynamics of the constitutive model calibrated from RO-IMR. The dashed curves correspond to the bubble dynamics of an inviscid fluid at the two length scales.

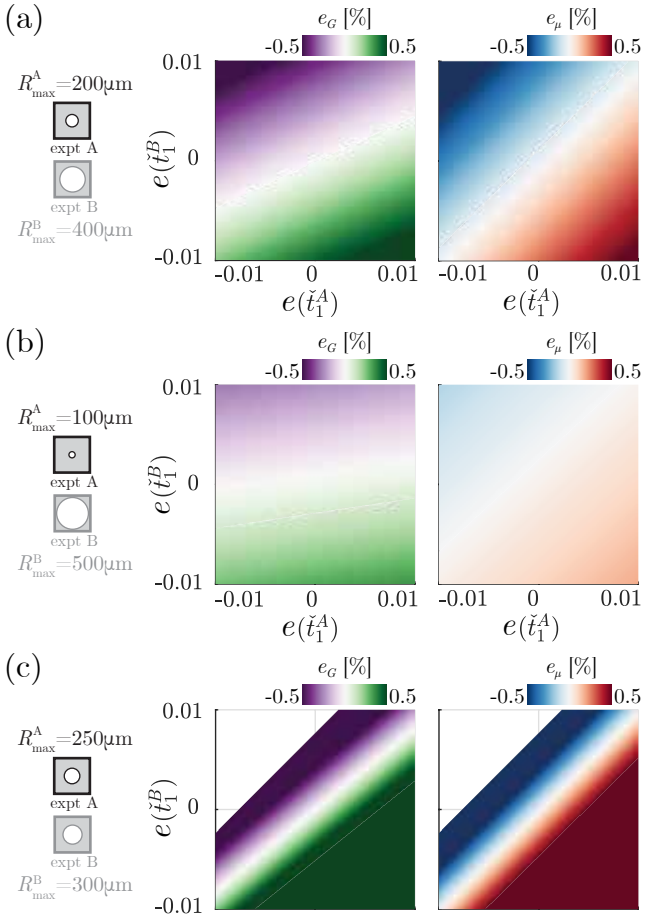

FIG. 10. Reproduction of simulated bubble dynamics for Kelvin-Voigt viscoelastic materials: effect of $\check{t}_1$ measurement error for different combinations of maximum radial length scales R_A and R_B of (a) {200, 400}μm, (b) {100, 500}μm, and (c) {250, 300}μm, respectively.

Kelvin-Voigt model with no fading memory. As α is decreased, the behavior of the springpot deviates from those of a pure Newtonian fluid, and the second peak amplitude $\hat{R}_2$ increases. Therefore, the trial value of α can be adjusted in a manner similar to the adjustment of τ_1 discussed above for the standard nonlinear solid model. An accurate estimate of α is thereby achieved by gradually narrowing down the range of possible values across multiple iterations, as shown in Figure 12. As shown in Table 5, the estimated values of viscoelastic parameters converge to the target values following additional iterations while the least-squares error also decreases.

B. Characterization from experimental data

To demonstrate the capability of the RO-IMR calibration approach to accelerate viscoelastic material characterziation, the procedure was applied to microcavitation experiments on polyacrylamide specimens. A total of $n = 5$ inertial cavitation experiments were performed on polyacrylamide specimens. The maximum radius $R_{\max}$ of the cavitated bubble ranged between 298.3 and 365.4 μm and the circumferential stretch of the bubble at peak radius ranged between 5.99 and 6.37. The measured bubble kinematics are shown in Fig. 13. The experiments were characterized to a Neo-Hookean Kelvin-Voigt model using standard IMR in least-squares fitting mode. Each forward simulation took approximately 30 s on a consumer personal laptop, on the order of 200 forward simulations are needed for calibration. The results for Neo-Hookean Kelvin-Voigt fitting are shown in Table 6. For the RO-IMR characterization procedure, six combinations of length scales were generated, in which the two experiments with smaller values of $R_{\max}$ (viz., Experiments 2 and 5) were grouped individually with the three experiments with larger values of $R_{\max}$ (viz., Experiments 1, 3, and 4).

A reduced-order fitting to the experiments is performed first for the finite deformation Kelvin-Voigt model. The two experiment combinations involving Experiment 4 were both found to result in negative values of viscous modulus μ. Accord-

TABLE 4. Iterative solution for standard nonlinear solid model example, $G = 4.8 \times 10^3$ Pa, $\mu = 0.109$ Pa s, $\tau_1 = 2.5 \times 10^{-6}$ s.

Iteration	Trial τ_1 [s]	Estimated G [Pa]	Estimated μ [Pa s]	Least-squares error, A	Least-squares error, B
1	0	3.806×10^3	5.139×10^{-2}	4.766	0.308
2	1.0×10^{-7}	3.832×10^3	4.860×10^{-2}	3.376	0.174
3	1.0×10^{-6}	4.077×10^3	6.165×10^{-2}	0.689	0.004
4	3.0×10^{-6}	4.602×10^3	9.495×10^{-2}	0.124	0.119
5	2.5×10^{-6}	4.477×10^3	8.609×10^{-2}	0.019	0.083

TABLE 5. Iterative solution for fractional Kelvin-Voigt model example, $G = 4.8 \times 10^3$ Pa, $\mu_\alpha = 0.327$ Pa s$^\alpha$, $\alpha = 0.86$.

Iteration	Trial α	Estimated G [Pa]	Estimated μ_α [Pa s$^\alpha$]	Least-squares error, A	Least-squares error, B
1	1	4.512×10^3	4.958×10^{-2}	4.787	2.337
2	0.9	4.739×10^3	1.878×10^{-1}	0.459	0.200
3	0.8	4.942×10^3	8.074×10^{-1}	0.415	0.336
4	0.86	4.784×10^3	3.256×10^{-1}	0.003	0.001

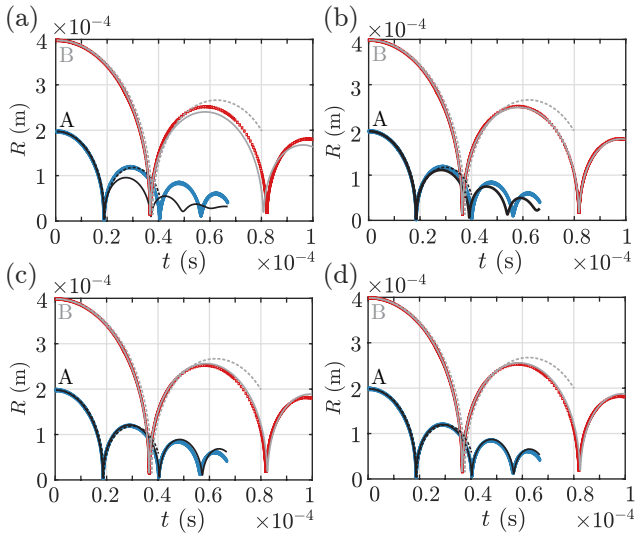

FIG. 11. Reproduction of simulated bubble dynamics for standard nonlinear solid viscoelastic materials by iterating value of relaxation time scale τ_1: (a) $\tau_1 = 0$, (b) $\tau_1 = 1 \times 10^{-6}$s, (c) $\tau_1 = 3 \times 10^{-6}$s, (d) $\tau_1 = 2.5 \times 10^{-7}$s. Blue circles denote the target bubble dynamics for length scale A and red squares denote the target bubble dynamics for length scale B. The solid curves are the bubble dynamics of the consitutive model calibrated from RO-IMR. The dashed curves correspond to the bubble dynamics of inviscid fluid at the two length scales.

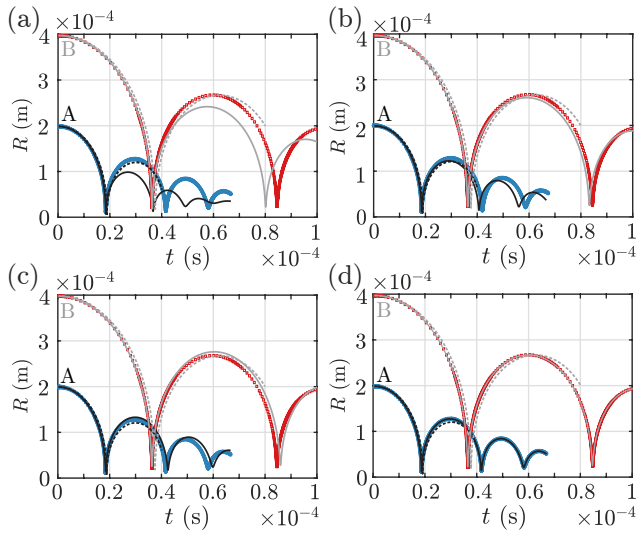

FIG. 12. Reproduction of simulated bubble dynamics for fractional Kelvin-Voigt viscoelastic materials by iterating value of relaxation time scale α: (a) $\alpha = 1$, (b) $\alpha = 0.9$, (c) $\alpha = 0.8$, (d) $\alpha = 0.86$. Blue circles denote the target bubble dynamics for length scale A and red squares denote the target bubble dynamics for length scale B. The solid curves are the bubble dynamics of the consitutive model calibrated from RO-IMR. The dashed curves correspond to the bubble dynamics of inviscid fluid at the two length scales.

ingly, we concluded that the initial collapse time measurement for Experiment 4 violated the scaling law—i.e., the viscous effect of the material increased with larger bubble size, resulting a negative solution for μ. The existence of non-physical solution to the RO-IMR procedure is also influenced by the fact that the length scales for the five experiments did not vary significantly, with the largest $R_{\max}$ being only 22.5% larger than the smallest case. As discussed earlier, the RO-IMR procedure is more sensitive to errors in $\check{t}_1$ measurement when $R^A_{\max}$ and $R^B_{\max}$ are closer to each other.

For the four remaining combinations of experiments, calibration for the standard nonlinear solid and fractional Kelvin-Voigt models were performed iteratively. The calibrated parameters and corresponding least-squares errors are summarized in Table 7. In general, the RO-IMR procedure successfully reproduces bubble dynamics with the initial collapse process and estimated collapse time matching well with the

TABLE 6. IMR best-fit parameter and least-squares error (LSQe) values for experiments 1-5 on polyacrylamide fit to a Neo-Hookean Kelvin-Voigt model.

Expt.	G [kPa]	μ [Pa s]	$\log_{10}$(LSQe)
1	13.8	0.17	−1.790
2	10.8	0.078	−1.746
3	12.5	0.14	−1.825
4	11.2	0.12	−1.832
5	13.0	0.11	−1.304

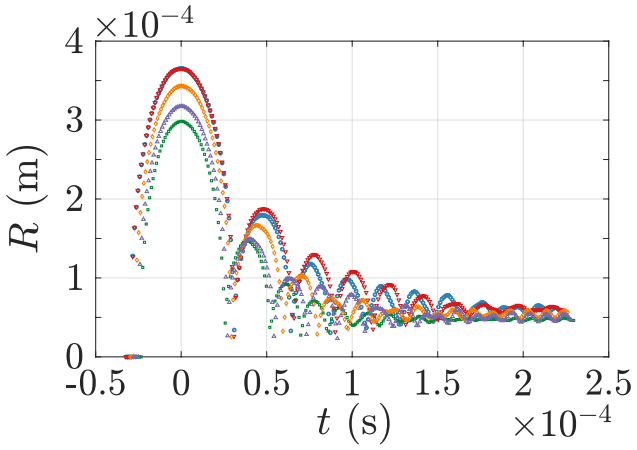

FIG. 13. Bubble dynamics measured from IMR experiments on polyacrylamide with concentration of 10/0.06% acrylamide/bisacrylamide.

shadowgraphy-estimated collapse time measurement. For all the experiments considered, the second peak $\hat{R}_2$ is underestimated by the calibrated Kelvin-Voigt model, suggesting non-negligible contribution from the fading memory of the material at the time scale investigated. Addition of Maxwell- and springpot-type relaxation mechanisms in the constitutive relation indeed improved the match of $\hat{R}_2$.

V. DISCUSSION

A. Non-monotonicity of cavitation kinematics

By harnessing viscoelastic models with more than two elements such as the standard nonlinear solid and fractional Kelvin-Voigt models, we improve the fidelity in prediction of high-rate behavior of soft polymers and biological tissues. The RO-IMR procedure introduced in the present work allows for such complex behaviors to be captured at a reduced computational cost. As shown previously by Estrada et al.[38], the Kelvin-Voigt model, consisting of a Neo-Hookean elastic response in parallel with a Newtonian viscous response, demonstrates monotonicity both in terms of collapse time and damping of bubble radius. Compared to the inviscid fluid case, a Neo-Hookean solid accelerates the initial collapse of the cavitated bubble and suppresses the peak magnitude of the bubble during later cycles of oscillation. In contrast, the Newtonian fluid model decelerates the initial collapse while also

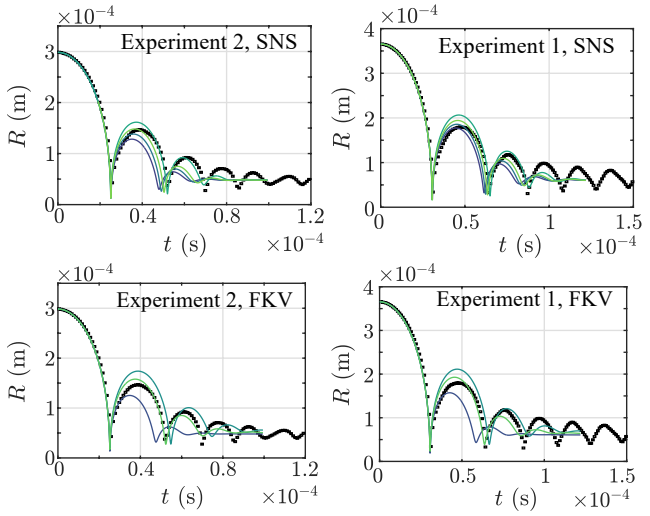

FIG. 14. RO calibration of standard nonlinear solid (a, b) and fractional Kelvin-Voigt (c, d) models for experiment combination 1. $R^A_{\max}$ = 298.3 µm for Experiment 2 (a, c), $R^B_{\max}$ = 365.4 µm for Experiment 1 (b, d). Black squares denote experimental data. Four iterations were performed, with the predicted bubble dynamics shown in lighter color for later iterations.

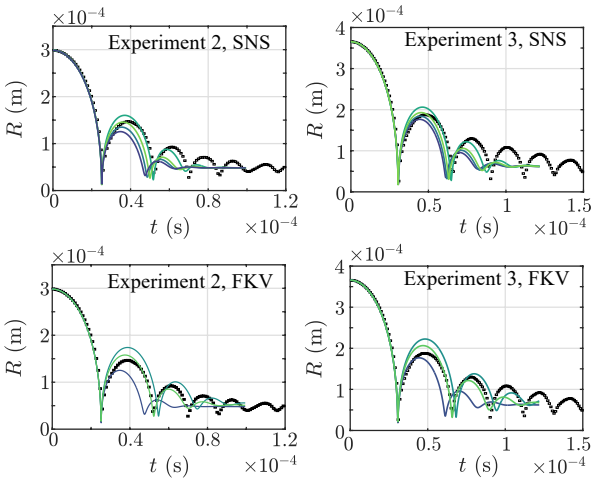

FIG. 15. RO calibration of standard nonlinear solid (a, b) and fractional Kelvin-Voigt (c, d) models for experiment combination 2. $R^A_{\max}$ = 298.3 µm for Experiment 2 (a, c), $R^B_{\max}$ = 365.2 µm for Experiment 3 (b, d). Black squares denote experimental data. Four iterations were performed, with the predicted bubble dynamics shown in lighter color for later iterations.

suppressing the peak magnitude of the bubble during later cycles.

Importantly, this decay behavior does not follow the same trend for either the standard nonlinear solid or the fractional Kelvin-Voigt model. Introduction of the Maxwell and springpot elements triggers non-monotonic kinematics due to fading memory of the material combined with the oscillatory nature of the inertial cavitation process. This is reflected in both the duration of the initial collapse and the magnitude of the bubble in later cycles of the oscillation process.

TABLE 7. Reduced-order viscoelastic model calibration from experiment data.

Combination	Viscoelastic model	G [kPa]	μ [Pa s$^{\alpha}$]	Least-squares error, A	Least-squares error, B
1	Kelvin-Voigt	15.56	0.144	0.248	0.085
	SNS, $\tau_1 = 1.0 \times 10^{-7}$ s	15.50	0.133	0.124	0.047
	SNS, $\tau_1 = 1.0 \times 10^{-6}$ s	16.00	0.159	0.049	0.109
	SNS, $\tau_1 = 3.2 \times 10^{-7}$ s	15.64	0.140	0.053	0.044
	FKV, $\alpha = 0.90$	14.76	0.415	0.211	0.366
	FKV, $\alpha = 0.95$	15.18	0.234	0.040	0.121
2	Kelvin-Voigt	16.04	0.154	0.306	0.213
	SNS, $\tau_1 = 1.0 \times 10^{-7}$ s	16.13	0.145	0.176	0.134
	SNS, $\tau_1 = 1.0 \times 10^{-6}$ s	16.65	0.172	0.046	0.066
	SNS, $\tau_1 = 3.2 \times 10^{-7}$ s	16.32	0.153	0.079	0.077
	FKV, $\alpha = 0.90$	15.41	0.458	0.169	0.213
	FKV, $\alpha = 0.95$	15.76	0.255	0.031	0.055
4	Kelvin-Voigt	18.15	0.208	0.438	0.372
	SNS, $\tau_1 = 1.0 \times 10^{-7}$ s	18.31	0.197	0.298	0.261
	SNS, $\tau_1 = 1.0 \times 10^{-6}$ s	19.04	0.233	0.081	0.079
	SNS, $\tau_1 = 3.2 \times 10^{-7}$ s	18.38	0.203	0.153	0.139
	FKV, $\alpha = 0.90$	17.16	0.610	0.170	0.158
	FKV, $\alpha = 0.95$	17.78	0.344	0.047	0.043
5	Kelvin-Voigt	18.86	0.222	0.511	0.654
	SNS, $\tau_1 = 1.0 \times 10^{-7}$ s	19.27	0.214	0.298	0.323
	SNS, $\tau_1 = 1.0 \times 10^{-6}$ s	20.23	0.256	0.081	0.101
	SNS, $\tau_1 = 3.2 \times 10^{-7}$ s	19.63	0.226	0.153	0.187
	FKV, $\alpha = 0.90$	18.16	0.676	0.121	0.068
	FKV, $\alpha = 0.95$	18.82	0.380	0.057	0.107

Fundamentally, the stress in the viscoelastic material reflects the material's resistance to distorting effects brought forth by the bubble kinematics. For a pure Neo-Hookean solid, the stress response resists the overall stretch of the material and encourages a recovery of the bubble radius to the equilibrium value of R_0. As a result, the initial collapse is accelerated by the presence of Neo-Hookean elasticity. For a pure Newtonian fluid, the stress response resists the instantaneous stretch rate. Consequentially, the Newtonian fluid decelerates the collapse process.

These competing effects interact meaningfully when the additional time scale(s) are introduced for the Maxwell and springpot elements. Specifically, the material has fading memory of past deformation states. As can be seen from the convolution integral form of constitutive relations (i.e., Equations 19 and 21), the stress response reflects a combined resistance to all historical stretch rate. When the material reaches the peak of initial expansion at $t = 0$ and begins its initial collapse, the fading memory of the material displays an overall resistance to its past expansion. That is, the material "remembers" the expanding trend that took place during $t < 0$. As a result, the collapse is initially accelerated by increased modulus (μ or μ_α). However, the material eventually develops more recent memories of the collapse process and its stress response transitions to one that decelerates the collapse. Thus, for Maxwell element or springpot that deviates only slightly from a Newtonian fluid (i.e., τ_1 close to 0 or α close to 1), the initial collapse time is still decelerated by higher viscous modulus. As the Maxwell and springpot elements behaves more elastically (i.e., large τ_1 or small α), the memory fades slower and the collapse time is accelerated by the viscous element for a longer period of time. Due to this effect from the fading memory, the scaling law for $\check{t}_1$ presented in Equations 41 and 42 is no longer effective for the moderate τ_1 or α cases at high modulus. As shown in Figures 6d, 7c, and 7d, the effectiveness of RO-IMR is limited to viscous modulus within a moderate range, approximately corresponding to $\mathrm{Re} > 10$ for the Maxwell model and $\mathrm{Ze} > 10$ for the springpot model.

Non-monotonicity is also observed for the peak magnitude of the bubble during the second oscillatory cycle, $\hat{R}_2$. When

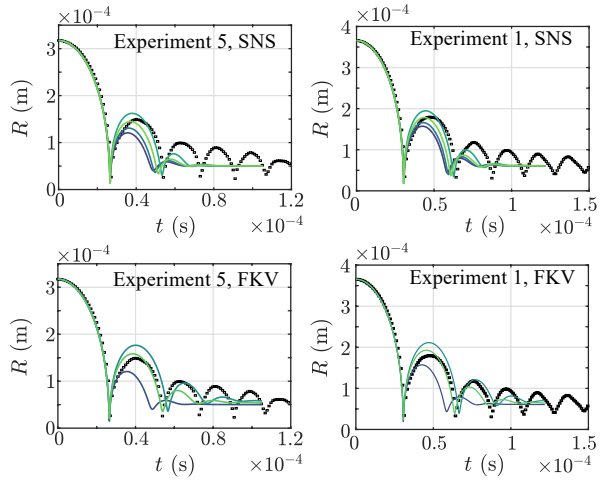

FIG. 16. RO calibration of standard nonlinear solid (a, b) and fractional Kelvin-Voigt (c, d) models for experiment combination 4. $R^A_{\max} = 317.5\,\mu$m for Experiment 5 (a, c), $R^B_{\max} = 365.4\,\mu$m for Experiment 1 (b, d). Black squares denote experimental data. Four iterations were performed, with the predicted bubble dynamics shown in lighter color for later iterations.

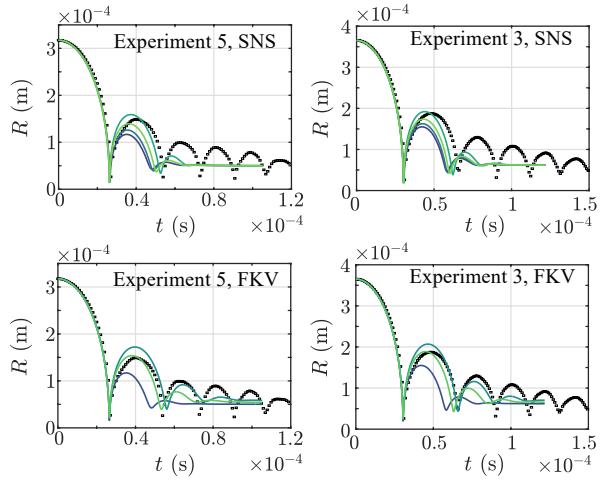

FIG. 17. RO calibration of standard nonlinear solid (top) and fractional Kelvin-Voigt (bottom) models for experiment combination 5. $R^A_{\max}$ = 317.5 μm for Experiment 5 (left), $R^B_{\max}$ = 365.2 μm for Experiment 3 (right). Black squares denote experimental data. Four iterations were performed, with the predicted bubble dynamics shown in lighter color for later iterations.

the viscous modulus is increased from zero to a moderate value, $\hat{R}_2$ increases. Once the modulus exceeds a critical value, further increase of the modulus leads to a decrease of $\hat{R}_2$. This trend is again due to the inherent time scale in the stress relaxation of the Maxwell and springpot elements. During the rebounding expansion taking place between $t = \check{t}_1$ and $t = \hat{t}_2$, a portion of the viscoelastic material "remembers" the previous collapse and generate a stress response to expand the bubble. As a result, the collapse is accelerated by higher material modulus, similar to the case of Neo-Hookean solid. For moderate values of τ_1 and α, increasing the material modulus will cause a transition of the overall collapse behavior from a viscous-like process to an elastic-like process. This is the cause of the collapse time scaling law failing for Maxwell element with large Re and springpot element with large Ze, as shown earlier in Figs. 6 and 7. The implication is thus that the secondary rebound amplitude may be a less straightforward quantity to use in higher-order RO modeling procedures.

B. Implications for data filtering and model identification

In addition to narrowing the range of viscoelastic parameters for material characterization, the RO approach allows for rapid filtering of experimental results and identification of data sets that are unsuitable for inverse characterization. In multiphase fluids and heterogeneous soft materials, local characterization leads to a varying spatial profile of mechanical behavior. However, collapse time irregularities can also occur for aspherical collapse due to the presence of boundaries or confounding experimental effects such as differential optical absorption of the material. In the original formulated IMR procedure, experiments with calibrated parameters that significantly deviate from those of other experiments could only be identified following extensive inverse characterization. In the RO-IMR setting, such comparisons between experiments could be quickly performed to correct the procedure.

Additionally, suitability of constitutive models can be identified rapidly with the help of the RO-IMR procedure. For example, the finite deformation Kelvin-Voigt model has been seen to underestimate the radius of bubble after the initial collapse. For characterized materials exhibiting fading memory behaviors during inertial cavitation, the mismatch of its bubble dynamics from that of a Kelvin-Voigt material can be discovered after a small number of simulations using the RO-IMR procedure, rather than performing an extensive amount of simulations to conclude the unsuitability of the constitutive model.

C. Effectiveness of the scaling law

According to information of initial collapse time ($\check{t}_1$) in the inertial cavitation of a Kelvin-Voigt type viscoelastic material, the presented RO-IMR procedure effectively estimates a pair of elastic and viscous moduli to describe soft viscoelastic hydrogels. The capability of the procedure was demonstrated for both the reproduction of simulated bubble dynamics using finite deformation Kelvin-Voigt, standard nonlinear solid, and fractional Kelvin-Voigt models, as well as experimental characterization of polyacrylamide specimens.

A basis of the RO approach is that initial collapse time of a viscoelastic material scales according to Equations 39 through 43. Since the proposed scaling law only concerns the initial collapse of the cavitated bubble, the viscoelastic model calibrated from the RO-IMR procedure is not guaranteed to accurately capture the bubble kinematics after the initial collapse. As illustrated in the Results section, a finite deformation Kelvin-Voigt model matching the initial collapse of

microcavitation experiments generally exhibits smaller bubble radius in later cycles than the experimental observations. The introduction of fading memory via the standard nonlinear solid and fractional Kelvin-Voigt allowed the later cycles of bubble oscillation to be captured with improved accuracy. This is due to the aforementioned non-monotonicity in cavitation kinematic response for fluids and soft materials with fading memory.

Yet, the ability of the RO-IMR procedure to match $\check{t}_1$ deteriorated for both the standard nonlinear solid and fractional Kelvin-Voigt models when compared to the Kelvin-Voigt model. As observed from Figs. 5, 6, and 7, the proposed scaling law is less effective for the Maxwell and springpot elements when compared to its performance for the Newtonian model without fading memory. As a result, the accuracy of the reduced-order inverse characterization is also less effective for the standard linear solid and fractional Kelvin-Voigt models without further refinement. An improved scaling law is needed to better reflect the dependence of $\check{t}_1$ on material parameters in these advanced viscoelastic models if rapid accuracy is required; however, we believe the method to be quite applicable to estimate initial state values for traditional optimization solvers.

For the polyacrylamide specimens characterized, we note that the best-fit Neo-Hookean Kelvin-Voigt models from our original IMR formulation systematically underestimated the elastic modulus. This can be expected for two principal reasons. First, an unweighted least-squares fitting procedure is biased by the number of data points included, which can serve to undercount certain physical metrics such as collapse time. By using the collapse time directly in the reduced-order approach, we perhaps orthogonalize the system as a characteristic time and decay behavior. In this particular case, the result is that the collapse time is tightened slightly, leading to a higher reduced-order estimate for the elastic modulus. Second, the fit to a Neo-Hookean Kelvin-Voigt model is likely conflating two or more concurrent time-scales of collapse. Coupled with the first point, the kinematic fit over longer times will result in combined elastic and viscous behaviors which result in consistent underfitting of the elastic behavior. Thus, we expect the use of quantities such as the collapse time to sharpen our estimate of actual material behavior from a physics-based standpoint.

D. Additional limitations

The reduced-order approach proposed here is a first attempt to accelerate the inverse characterization process of viscoelastic materials with the IMR experimental technique. Though significant improvement is observed in the efficiency of model calibration, several limitations still exist in the present approach.

The application of RO-IMR to inversely characterize polyacrylamide specimens from microcavitation experiments revealed the sensitivity of the proposed method to uncertainty of the primary collapse time, $\check{t}_1$, necessitating an experimental improvement to accurately assess this time. For the microcavitation experiments conducted in the present study, the initial collapse time typically ranged between 25 to 31 microseconds. Using high speed camera paired with shadowgraphy and multi-strobing, we were able to reduce the error bound of the collapse time to fractions of microseconds. However, as shown in Figures 9 and 10, even minor inaccuracy of the $\check{t}_1^A$ and $\check{t}_1^B$ results in a departure from Equation 45, which is in turn amplified by using pair of experiments with comparable $R_{\max}^A$ and $R_{\max}^B$. Due to the need for bubble sphericity, the upper bound of bubble size is limited by the size of our cuvettes, while the minimum size is practically limited by a triumverate combination of the numerical aperture of the converging optical objective, laser profile, and requirement to see the emitted shockwave on collapse for time-assessment. Thus, the length scales in the experiments presented here are within a moderate range, with $R_{\max}^B/R_{\max}^A < 1.3$ for all combinations examined. As a result, a solution was unable to be achieved in some pairs of experiments (viz., Combinations 3 and 6). The effectiveness of the RO-IMR procedure would benefit from further experimental refinement to increase the range of $R_{\max}$ that can satisfy our range of constraints.

Since the RO-IMR procedure fundamentally considers the ratio between the collapse times of a viscoelastic material and an inviscid fluid at two different length scales, as seen in Equation 45, errors in the measurement of the bubble collapse time becomes amplified when it is very close to the collapse time in an inviscid fluid. That is, when $\check{t}_1 \approx \check{t}_1^{inv}$, errors in the measurement of $\check{t}_1$ drastically alters the quantity $\left[1-\left(\check{t}_1^{inv}/\check{t}_1\right)^2\right]$. In future applications of the RO-IMR procedure, the size scale of the cavitated bubble can be perhaps optimized according to initial estimate of the viscoelastic parameters and experimental constraints, such that a pair of "strongly elastic" and "strongly viscous" experiments can be achieved—i.e., a collapse time sufficiently shorter than the inviscid case at the larger length scale and a collpase time sufficiently longer than the inviscid case at the smaller length scale.

VI. CONCLUSION

The RO-IMR procedure presented herein allows for accelerated characterization of local viscoelastic properties of soft materials at ultra-high strain rates up to 10^8 s^{-1}. Through reproduction of target simulations and experimental characterization of polyacrylamide specimens, we have demonstrated that the proposed procedure effectively pare down the space upon which we seek the global minima of viscoelastic model parameters. The effectiveness of the proposed approach to calibrate advanced Kelvin-Voigt type material models (standard nonlinear solid and fractional Kelvin-Voigt) also demonstrate the capability of this framework to capture the complex time-dependent behaviors observed in soft biological materials. We envision that this improvement in the computational cost of IMR will significantly broaden its applicability to understand the viscoelasticity of polymeric materials and biological tissues subjected to high-rate localized deformation.

VII. ACKNOWLEDGEMENTS

JBE would like to gratefully acknowledge the Haythornthwaite Foundation for providing financial support for this work.

VIII. DATA AVAILABILITY

All data will be made available at in the Deep Blue Data repository hosted at the University of Michigan. All data in the repository will be available for anyone to download without restriction and will be licensed under a Creative Commons 4.0 license.

[1]M. S. Plesset, "The dynamics of cavitation bubbles," Journal of Applied Mechanics **16**, 277–282 (1949).
[2]J. B. Keller and M. Miksis, "Bubble oscillations of large amplitude," The Journal of the Acoustical Society of America **68**, 628–633 (1980).
[3]R. Nigmatulin, N. Khabeev, and F. Nagiev, "Dynamics, heat and mass transfer of vapour-gas bubbles in a liquid," International Journal of Heat and Mass Transfer **24**, 1033–1044 (1981).
[4]W. Kreider, L. A. Crum, M. R. Bailey, and O. A. Sapozhnikov, "A reduced-order, single-bubble cavitation model with applications to therapeutic ultrasound," The Journal of the Acoustical Society of America **130**, 3511–3530 (2011).
[5]A. Prosperetti, L. A. Crum, and K. W. Commander, "Nonlinear bubble dynamics," The Journal of the Acoustical Society of America **83**, 502–514 (1988).
[6]R. L. Street and B. E. Larock, "Two models for cavity flow—a theoretical summary and applications," Journal of Basic Engineering (1968).
[7]H. S. Fogler and J. D. Goddard, "Collapse of spherical cavities in viscoelastic fluids," The Physics of Fluids **13**, 1135–1141 (1970).
[8]I. Tanasawa and W.-J. Yang, "Dynamic behavior of a gas bubble in viscoelastic liquids," Journal of Applied Physics **41**, 4526–4531 (1970).
[9]C. E. Brennen, *Cavitation and bubble dynamics* (Cambridge University Press, 2014).
[10]C. E. Brennen, "Cavitation in medicine," Interface focus **5**, 20150022 (2015).
[11]M. R. Bailey, R. O. Cleveland, T. Colonius, L. A. Crum, A. P. Evan, J. E. Lingeman, J. A. McAteer, O. A. Sapozhnikov, and J. Williams, "Cavitation in shock wave lithotripsy: the critical role of bubble activity in stone breakage and kidney trauma," in *IEEE Symposium on Ultrasonics, 2003*, Vol. 1 (IEEE, 2003) pp. 724–727.
[12]Z. Xu, J. B. Fowlkes, E. D. Rothman, A. M. Levin, and C. A. Cain, "Controlled ultrasound tissue erosion: The role of dynamic interaction between insonation and microbubble activity," The Journal of the acoustical Society of America **117**, 424–435 (2005).
[13]J. E. Parsons, C. A. Cain, G. D. Abrams, and J. B. Fowlkes, "Pulsed cavitational ultrasound therapy for controlled tissue homogenization," Ultrasound in medicine & biology **32**, 115–129 (2006).
[14]K.-M. Shyue, "An efficient shock-capturing algorithm for compressible multicomponent problems," Journal of Computational Physics **142**, 208–242 (1998).
[15]R. Saurel and R. Abgrall, "A multiphase godunov method for compressible multifluid and multiphase flows," Journal of Computational Physics **150**, 425–467 (1999).
[16]R. Abgrall, "How to prevent pressure oscillations in multicomponent flow calculations: a quasi conservative approach," Journal of Computational Physics **125**, 150–160 (1996).
[17]G.-S. Jiang and C.-W. Shu, "Efficient implementation of weighted eno schemes," Journal of computational physics **126**, 202–228 (1996).
[18]E. Johnsen and T. Colonius, "Implementation of WENO schemes in compressible multicomponent flow problems," J. Comput. Phys. **219**, 715–732 (2006).
[19]V. Coralic and T. Colonius, "Shock-induced collapse of a bubble inside a deformable vessel," European Journal of Mechanics-B/Fluids **40**, 64–74 (2013).
[20]S. A. Beig and E. Johnsen, "Maintaining interface equilibrium conditions in compressible multiphase flows using interface capturing," Journal of Computational Physics **302**, 548–566 (2015).
[21]M. Rodriguez, E. Johnsen, and K. G. Powell, "A high-order accurate AUSM + -up approach for simulations of compressible multiphase flows with linear viscoelasticity," Shock Waves **29**, 717–734 (2019).
[22]S. H. Bryngelson, K. Schmidmayer, V. Coralic, J. C. Meng, K. Maeda, and T. Colonius, "MFC: An open-source high-order multi-component, multiphase, and multi-scale compressible flow solver," Comput. Phys. Commun. , 107396 (2020).
[23]M. Rodriguez and E. Johnsen, "A high-order accurate five-equations compressible multiphase approach for viscoelastic fluids and solids with relaxation and elasticity," J. Comput. Phys. **379**, 70–90 (2019).
[24]J. W. Strutt, "Viii. on the pressure developed in a liquid during the collapse of a spherical cavity," The London, Edinburgh, and Dublin Philosophical Magazine and Journal of Science **34**, 94–98 (1917).

[25] X. Yang and C. C. Church, "A model for the dynamics of gas bubbles in soft tissue," The Journal of the Acoustical Society of America **118**, 3595–3606 (2005).
[26] C. Hua and E. Johnsen, "Nonlinear oscillations following the rayleigh collapse of a gas bubble in a linear viscoelastic (tissue-like) medium," Physics of Fluids **25**, 083101 (2013).
[27] J. S. Allen and R. A. Roy, "Dynamics of gas bubbles in viscoelastic fluids. ii. nonlinear viscoelasticity," The Journal of the Acoustical Society of America **108**, 1640–1650 (2000).
[28] M. Warnez and E. Johnsen, "Numerical modeling of bubble dynamics in viscoelastic media with relaxation," Physics of Fluids **27**, 063103 (2015).
[29] R. Gaudron, M. Warnez, and E. Johnsen, "Bubble dynamics in a viscoelastic medium with nonlinear elasticity," Journal of Fluid Mechanics **766** (2015).
[30] J. Yang, H. C. Cramer III, and C. Franck, "Extracting non-linear viscoelastic material properties from violently-collapsing cavitation bubbles," Extreme Mechanics Letters **39**, 100839 (2020).
[31] J. A. Zimberlin, N. Sanabria-DeLong, G. N. Tew, and A. J. Crosby, "Cavitation rheology for soft materials," Soft Matter **3**, 763–767 (2007).
[32] S. Kundu and A. J. Crosby, "Cavitation and fracture behavior of polyacrylamide hydrogels," Soft Matter **5**, 3963–3968 (2009).
[33] J. A. Zimberlin, J. J. McManus, and A. J. Crosby, "Cavitation rheology of the vitreous: mechanical properties of biological tissue," Soft Matter **6**, 3632–3635 (2010).
[34] A. Blumlein, N. Williams, and J. J. McManus, "The mechanical properties of individual cell spheroids," Scientific Reports **7**, 1–10 (2017).
[35] M. P. Milner and S. B. Hutchens, "A device to fracture soft solids at high speeds," Extreme Mechanics Letters **28**, 69–75 (2019).
[36] M. P. Milner and S. B. Hutchens, "Multi-crack formation in soft solids during high rate cavity expansion," Mechanics of Materials **154**, 103741 (2021).
[37] S. Chockalingam, C. Roth, T. Henzel, and T. Cohen, "Probing local nonlinear viscoelastic properties in soft materials," Journal of the Mechanics and Physics of Solids , 104172 (2020).
[38] J. B. Estrada, C. Barajas, D. L. Henann, E. Johnsen, and C. Franck, "High strain-rate soft material characterization via inertial cavitation," Journal of the Mechanics and Physics of Solids **112**, 291–317 (2018).
[39] C. Barajas and E. Johnsen, "The effects of heat and mass diffusion on freely oscillating bubbles in a viscoelastic, tissue-like medium," The Journal of the Acoustical Society of America **141**, 908–918 (2017).
[40] A. Bonfanti, J. L. Kaplan, G. Charras, and A. Kabla, "Fractional viscoelastic models for power-law materials," Soft Matter **16**, 6002–6020 (2020).
[41] I. Akhatov, O. Lindau, A. Topolnikov, R. Mettin, N. Vakhitova, and W. Lauterborn, "Collapse and rebound of a laser-induced cavitation bubble," Physics of Fluids **13**, 2805–2819 (2001).
[42] J. Zhu, T. Li, S. Cai, and Z. Suo, "Snap-through expansion of a gas bubble in an elastomer," The Journal of Adhesion **87**, 466–481 (2011).
[43] H. Hencky, "Uber die form des elastizitatsgesetzes bei ideal elastischen stoffen," Zeit. Tech. Phys. **9**, 215–220 (1928).
[44] H. Hencky, "The law of elasticity for isotropic and quasi-isotropic substances by finite deformations," Journal of Rheology (1929-1932) **2**, 169–176 (1931).
[45] G. A. Holzapfel, *Nonlinear solid mechanics: a continuum approach for engineering science* (John Wiley & Sons, Inc., 2000).
[46] M. Bouzid, B. Keshavarz, M. Geri, T. Divoux, E. Del Gado, and G. H. McKinley, "Computing the linear viscoelastic properties of soft gels using an optimally windowed chirp protocol," Journal of Rheology **62**, 1037–1050 (2018).
[47] M. D. Choudhury, S. Chandra, S. Nag, S. Das, and S. Tarafdar, "Forced spreading and rheology of starch gel: Viscoelastic modeling with fractional calculus," Colloids and Surfaces A: Physicochemical and Engineering Aspects **407**, 64–70 (2012).
[48] F. Meral, T. Royston, and R. Magin, "Fractional calculus in viscoelasticity: an experimental study," Communications in nonlinear science and numerical simulation **15**, 939–945 (2010).
[49] M. Zhang, P. Nigwekar, B. Castaneda, K. Hoyt, J. V. Joseph, A. di Sant'Agnese, E. M. Messing, J. G. Strang, D. J. Rubens, and K. J. Parker, "Quantitative characterization of viscoelastic properties of human prostate correlated with histology," Ultrasound in medicine & biology **34**, 1033–1042 (2008).
[50] M. Z. Kiss, T. Varghese, and T. J. Hall, "Viscoelastic characterization of in vitro canine tissue," Physics in Medicine & Biology **49**, 4207 (2004).
[51] W. Zhang, A. Capilnasiu, G. Sommer, G. A. Holzapfel, and D. A. Nordsletten, "An efficient and accurate method for modeling nonlinear fractional viscoelastic biomaterials," Computer Methods in Applied Mechanics and Engineering **362**, 112834 (2020).
[52] M. Caputo, "Linear models of dissipation whose q is almost frequency independent—ii," Geophysical Journal International **13**, 529–539 (1967).
[53] M. Caputo and F. Mainardi, "A new dissipation model based on memory mechanism," Pure and applied Geophysics **91**, 134–147 (1971).
[54] P. Haupt and A. Lion, "On finite linear viscoelasticity of incompressible isotropic materials," Acta Mechanica **159**, 87–124 (2002).
[55] Y.-N. Zhang, Z.-Z. Sun, and H.-L. Liao, "Finite difference methods for the time fractional diffusion equation on non-uniform meshes," Journal of Computational Physics **265**, 195–210 (2014).
[56] E. Kreyszig, "Advanced engineering mathematics," (John Wiley & Sons, Inc., 2011) Chap. 19, 10th ed.
[57] P. Quinto-Su, X. Huang, S. Gonzalez-Avila, T. Wu, and C. Ohl, "Manipulation and microrheology of carbon nanotubes with laser-induced cavitation bubbles," Physical review letters **104**, 014501 (2010).
[58] E. Traldi, M. Boselli, E. Simoncelli, A. Stancampiano, M. Gherardi, V. Colombo, and G. S. Settles, "Schlieren imaging: a powerful tool for atmospheric plasma diagnostic," EPJ Techniques and Instrumentation **5**, 1–23 (2018).
[59] V. Agrež, T. Požar, *et al.*, "High-speed photography of shock waves with an adaptive illumination," Optics letters **45**, 1547–1550 (2020).
[60] J. R. Tse and A. J. Engler, "Preparation of hydrogel substrates with tunable mechanical properties," Current protocols in cell biology **47**, 10–16 (2010).
[61] C.-D. Ohl, T. Kurz, R. Geisler, O. Lindau, and W. Lauterborn, "Bubble dynamics, shock waves and sonoluminescence," Philosophical Transactions of the Royal Society of London. Series A: Mathematical, Physical and Engineering Sciences **357**, 269–294 (1999).
[62] O. Lindau and W. Lauterborn, "Cinematographic observation of the collapse and rebound of a laser-produced cavitation bubble near a wall," Journal of Fluid Mechanics **479**, 327–348 (2003).
[63] O. Supponen, D. Obreschkow, P. Kobel, M. Tinguely, N. Dorsaz, and M. Farhat, "Shock waves from nonspherical cavitation bubbles," Physical Review Fluids **2**, 093601 (2017).